Bandgap Engineering and Doping in ZnCdO Thin Films

March 2022

Department of Science and Advanced Technology

Graduate School of Science and Engineering

Saga University

Hyochang Jang

Bandgap Engineering and Doping in ZnCdO Thin Films

Abstract

Transparent conducting oxides (TCOs) are one of the key components of a solar cell to collect charge carriers from the illuminated side of the cell. In order to achieve high conversion efficiency, TCOs that can transmit light in a wide range of wavelengths is required. However, widely used TCOs such as In_2O_3: Sn (ITO), In_2O_3:Ga (IGO), and ZnO:Al (AZO) have limited transmittance in the IR region (>1000 nm) because of their high electron concentration (> 10^{21} cm^{-3}) and low mobility (< 40 cm^2/Vs) which give rise to strong free carrier absorption (FCA) and plasma reflection. Therefore, the research to find new TCO materials with high transmittance extending into the IR region (> 1500 nm) are essential for full solar spectrum photovoltaics.

Among the various TCO material candidates, CdO has the highest reported mobility values of 200 cm^2/Vs at an electron concentration > 10^{21} cm^{-3}, and thus has been considered as a promising candidate for full spectrum solar cell applications. Because of the high mobility, CdO is expected to realize a low resistive thin film with a low carrier concentration, extending the FCA and a plasma reflection effect to a much longer

wavelength region (λ > 2000 nm). Hence it can be used as transparent conductors on devices in which transparency in the long wavelength infrared region is required. Although the band gap (2.3 eV) of CdO is small for a transparent conductor application, it can be increased by alloying with a larger gap oxide such as ZnO which has a band gap of ~ 3.3 eV. However, because ZnO has a wurtzite (WZ) structure (α=3.25 Å, c=5.21 Å) whereas CdO a rocksalt (RS) structure (α=4.70 Å), the crystal structure of $Zn_{1-x}Cd_xO$ (ZnCdO) is expected to change at a certain Cd composition. However, reported ZnCdO thin films shows lower band gap compared to other TCOs materials. Therefore, this research mainly focused on expanding the band gap of ZnCdO thin films to absorb much more sun spectrum, archiving higher conversion efficiency

This dissertation explores the optical, structural, and electrical properties of ZnCdO thin film alloys ($0 \leq x \leq 1$) grown by molecular beam epitaxy under various growth condition.

At the beginning of this research, ZnCdO thin films are grown on sapphire substrate by MBE with various Cd compositions for studying structural, electrical, and optical properties of ZnCdO thin films. The phase transition from WZ to RS is found to take a place at the Cd content x ~ 0.5 to 0.6. Within the composition region of x ~ 0.5 to 0.6, both RS and WZ crystals co-exist. Transmittance above 80 ~ 95 % in the visible range is

observed for both the WZ and RS alloys. Optical gap of the WZ alloys decreases from 3.27 eV for ZnO to ~ 2.35 eV (x ~ 0.44). At the phase transition to RS at x ~ 0.55, the optical gap increases drastically to > 3.0 eV RS-alloys with a large optical gap of 3.0 eV (an intrinsic gap of ~ 2.7 eV) is achieved for x ~ 0.6. RS-ZnCdO thin films exhibit a low resistivity of 5×10^{-4} Ωcm with maximum mobility of ~ 90 cm^2/Vs and a high carrier concentration 4×10^{20} cm^{-3}.

Secondly, the sapphire substrate is replaced with MgO (100) substrate to improve the crystallinity and increase the bandgap of RS-ZnCdO thin films. It is found that the phase transition from WZ to RS occurs at the Cd composition x between 0.51 and 0.59, and RS-ZnCdO is epitaxially grown on MgO (100) at the Cd composition x above 0.59. In the visible range, high transmittance above 85% is observed for RS-ZnCdO films ($0.59 \leq x \leq 1.0$). In the WZ-phase region, the optical band gap energy decreases from 3.25 eV for ZnO to ~ 2.16 eV for WZ-ZnCdO with x ~ 0.51. After the partial phase transition from WZ to RS at x > 0.51, the optical band gap energy increases intensely and the largest optical band gap energy of 3.08 eV is obtained for x =0.59 with an intrinsic band gap energy of 2.72 eV. RS-ZnCdO films shows a low resistivity around 2.5×10^{-4} Ωcm with a maximum mobility of ~ 51.7 cm^2/Vs and a high carrier concentration around 5×10^{20} cm^{-3}.

Finally, in order to further increase the band gap energy of ZnCdO, the effects of Al doping on the structural, electrical, and optical properties of RS-ZnCdO thin films on MgO substrates are investigated. The electron concentration increases with increasing Al cell temperature T_{Al}, and is n~1.5×10^{21} cm^{-3} at T_{Al} = 875 °C, which corresponds to an Al-doping concentration of ~7.8%. The corresponding optical band gap energy increases because of free-carrier effects including Burstein-Moss-shift and band-renormalization. Furthermore, Al is an efficient donor dopant in both RS-ZnCdO and WZ-ZnCdO thin films. Electron concentrations $>10^{21}$ cm^{-3} are obtained with Al doping for alloys incorporating Cd content x ranging from 0.27 to 1.0, regardless of the crystal structure. A large optical band gap energy of 3.45 eV is observed in the RS-ZnCdO thin film having $x\approx0.7$, with a resistivity of 1×10^{-4} Ω-cm, and a wide transmission window of up to 2000 nm. These characteristics of RS-ZnCdO are attractive as TCO materials in future full spectrum solar cells.

TABLE OF CONTENTS

Chapter 1

Introduction

1.1 Introduction

Recently, environmental pollution has become serious globally, and research to reduce it has been actively developed. Among them, research about global warming is becoming most attractive nowadays [1]. Global warming is caused due to the increase of greenhouse gases such as methane or propane gases and carbon dioxide in the atmosphere. Carbon dioxide charges the

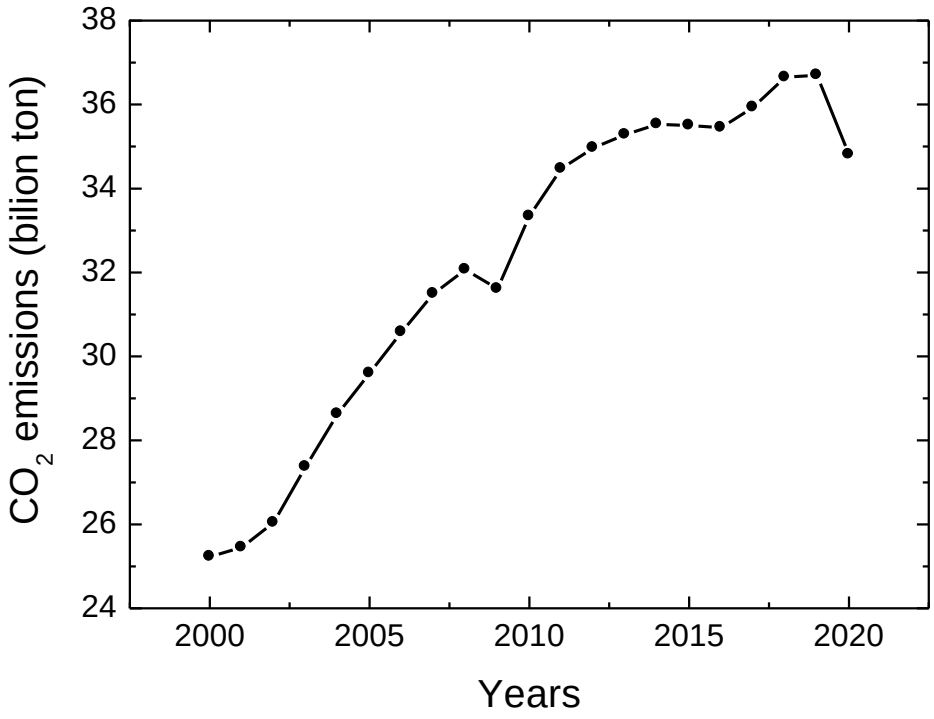

Figure 1.1 Carbon dioxide emissions from the burning of fossil fuels for energy and cements production from the Global Carbon Project.

most of greenhouse gases. According to the report of Robbie Andrew [2], fossil CO_2 emissions of a global world and national is gradually increased and reached 34.7 billion tons in 2020 as shown in Fig. 1.1.

The most significant amount of carbon dioxide (CO_2) is produced by the combustion of fossil fuels [3], which is the most significant part of energy in modern life. Therefore, the need for research and policies to reduce carbon dioxide is growing and increasing. As a solution to such environmental pollution, research on renewable energy like wind power generation [4], hydroelectric power generation, and photovoltaic power generation [5], which are eco-friendly energy generations, has been conducted worldwide.

According to the global average annual energy investment reported by World Energy Outlook 2019 [6], among the investments from 2014 to 2018, coal was reported as 7%, 19% for natural gas, 25% for oil, and 17% for renewable energy as shown in Fig. 1.2. In addition, according to the investment scenarios goals from 2019 to 2040, coal decreased 2%, and oil decreased to 18%, but renewable energy increased to 25%. As such, policies to reduce environmental pollution

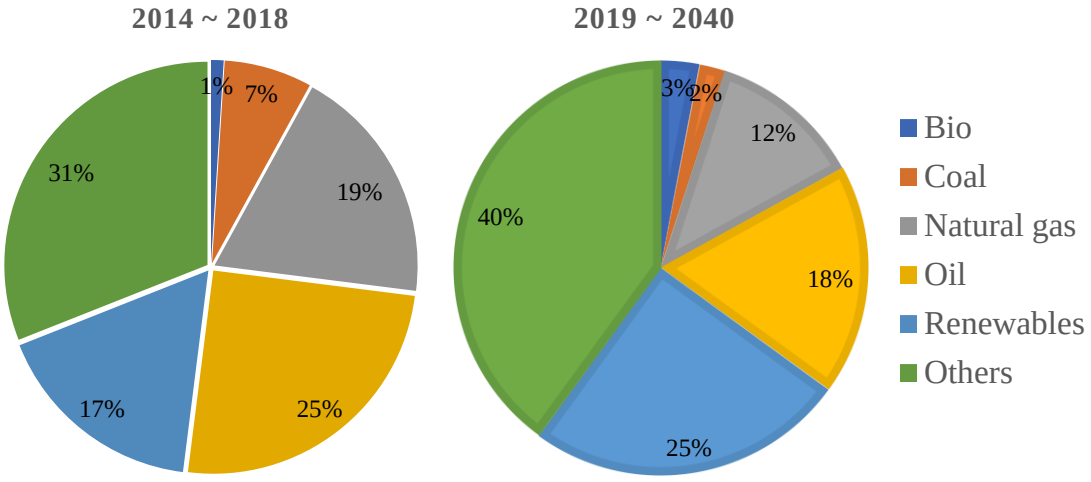

Figure 1.2 Global average annual energy supply investment by type and scenario from by World Energy Outlook 2019.

increase worldwide by reducing fossil fuels and natural gas, furthermore, using nature-friendly energy by developing renewable energy.

Figure 1.3 shows the reported state's policies for the global installed power generation capacity scenario from the world energy outlook 2019. The most remarkable thing is that solar photovoltaic power accounts for more global installed capacity than any other energy source by the late 2020s to mid-2030s, depending on the scenario. One of the most attractive advantages of photovoltaic power generation is that solar energy is directly converted into electric energy by solar cells, which means that the energy source is unlimited and the adverse effects on the environment are small [7, 8]. Therefore, solar photovoltaic can be a responsible candidate for the future of energy. In this chapter, the principle and the current states of solar cells are explained.

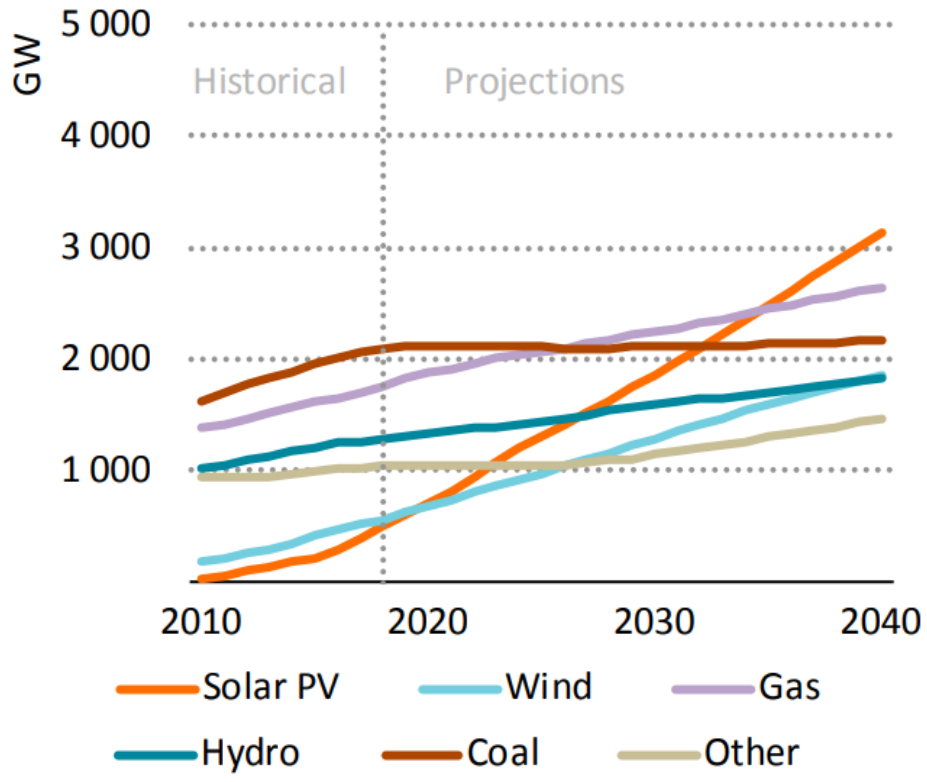

Figure 1.3 Global installed power generation capacity by scenario from the World Energy Outlook 2019.

1.2 History of solar cell

The Earth receives 174 PW of solar radiation above the Earth's atmosphere. About 30% bounce back into space, but the rest seeps into the atmosphere, sea, and land. Solar cells can convert those atmospheric solar radiation energies into electrical energy that we can use for daily life.

Solar cells are devices that convert sun spectra into direct electric current using photoelectric effects. Charles Fritts assembled the first solar cell in the 1880s. Russell Ohl in the 1940s and Daryl Chapin et al. in 1954 developed silicon solar cells. These early solar cells cost 286 USD per watt and reached 4.5 to 6% efficiency. As such, solar cells in the early days were expensive and showed low conversion efficiency. However, the highest conversion efficiency of 50 ~ 52 % was achieved through repeated developments on recent reports in the National Renewable Energy Laboratory (NREL) [9].

Solar cells are fabricated using semiconducting materials and based on photovoltaic effects. When light having energy equal to or greater than the semiconductor's band gap is irradiated to the material, electrons are excited from the valence band to the conduction band and generate energy through an external circuit.

However, there are many disadvantages too, because of the low efficiency and relatively high production costs, the need for a large land area to produce large quantities of electricity, and the discontinuity of sunlight. Therefore, it needs much more research.

1.3 The principle of solar cells

As mentioned in **Chapter 1.2**, a solar cell is a photovoltaic cell designed to convert solar energy into electrical energy using the photovoltaic effect. The photovoltaic effect is a process that generates a voltage or electric current in a photovoltaic cell when it is exposed to sunlight. The photovoltaic effect was first discovered in 1839 by Edmond Becquerel. When doing experiments involving wet cells, he noted that the cell's voltage increased when its silver plates were exposed to the sunlight [10].

Solar cells generate electrons with that photovoltaic effect on the *pn* junction semiconductor. The process of the current generation in the solar cell is explained as follows [11, 12].

I. *pn* junction semiconductor solar cell is fabricated by contacting of *p*-type and *n*-type semiconductor. Generally, phosphorus doped for *n*-type and boron doped *p*-type silicon semiconductors are used. The *n*-type film is thin to allow light to pass through to the *pn* junction.

II. As the *n*-type material has lost electrons and the *p*-type has lost holes, an electric field across the *pn* interface is established. Due to this electric field, electrons on *n*-type and holes on *p*-type are recombined, and a depletion zone is built at the *pn* junction interface.

III. When light is illuminated to the solar cell face, electrons and hole in the semiconductor are excited to move freely within the diffusion length. The collection of light-generated

carriers by the *pn* junction causes a movement of electrons to the *n*-type side and holes to the *p*-type side of the junction.

IV. When they enter the region with the electric field, the electrons are collected in the *n*-type semiconductor, and the holes are collected in the *p*-type semiconductor.

V. When an electrode is formed on the *p*-type surface, the *n*-type semiconductors and electrons flow to the external circuit, generating a current.

1.4 Current states of solar cells

There are many types of solar cells like silicon solar cells, compound semiconductor solar cells, and tandem solar cells, depending on the materials and structure. Among the most widely used ones is the silicon solar cell.

Silicon solar cells are classified into first-generation bulk solar cells and second-generation thin-film solar cells. First-generation bulk solar cells include single-crystalline silicon and poly-crystalline silicon solar cells.

Single-crystalline silicon is obtained by melting the silica with high purity and then mono crystallizing by the Czochralski(CZ) process or floating zone method. The CZ process involves heating and melting poly-crystalline silicon in a crucible, contacting the single-crystalline seeds into the melt surface, and gradually raising the seeds to grow a single-crystalline at the tip of the seed to form a thick rod. Currently, about 90% of the production of single-crystalline silicon is

made by the CZ method [13]. The resulting silicon ingot is cut, polished, and cleaned to a thin plate-like silicon wafer.

The single-crystalline silicon solar cells are fabricated on the single-crystalline wafer [14]. Single-crystalline silicon solar cells have a high conversion efficiency. Therefore, single-crystalline silicon solar cells are used the most widely and have the longest history of currently used solar cells globally. However, it has disadvantages: it is expensive to produce high purity and low defect of single-crystalline silicon.

Poly-crystalline silicon solar cells are manufactured using extra materials or lower grade silicon or raw materials produced during the manufacturing process of other silicon semiconductor devices [15]. Although it has a disadvantage of low conversion efficiency compared to single-crystalline silicon solar cells, it is widely used because of its low production cost and its balance that performance is not so bad compared with single-crystalline silicon.

Solar cells fabricated using III-V compound semiconductors such as GaAs and InP are expected to have high conversion efficiencies of 30% to 40% [16]. However, since these materials have a high substrate cost and a high process cost, it is mainly used as a space or a concentrator photovoltaics applications in the present state.

On the other hand, a thin film solar cell refers to a solar cell having a semiconductor layer with a thickness of several micrometers. Thin film solar cells include amorphous silicon solar cells, II-VI compound thin films, or I-III-VI_2 compound thin film solar cells.

The amorphous silicon solar cells are manufactured in a completely different method from the crystalline silicon solar cell. Silicon containing gas as source material is injected into the

vacuum chamber, and a high-frequency discharge is performed to form a thin film on the glass substrate [17]. As a result, the amount of silicon material used is small. Furthermore, the energy efficiency of amorphous silicon solar cells is good, and the manufacturing cost is low. However, there is a disadvantage that the amorphous silicon solar cell is easy to take light degradation.

CdTe, II-VI compound semiconductor, has a high conversion efficiency and has become a highly efficient material as a thin film.

Solar cells have been studied in many ways to achieve high efficiency with low manufacturing costs. For example, multi-junction solar cell has been investigated as shown in Fig. 1.4. Multi-junction solar cell is fabricated with different semiconductor materials to absorb broader range of wavelengths, improving the solar cell's conversion efficiency. Therefore, the importance of transparent conducting oxides has been increased to achieve higher performance.

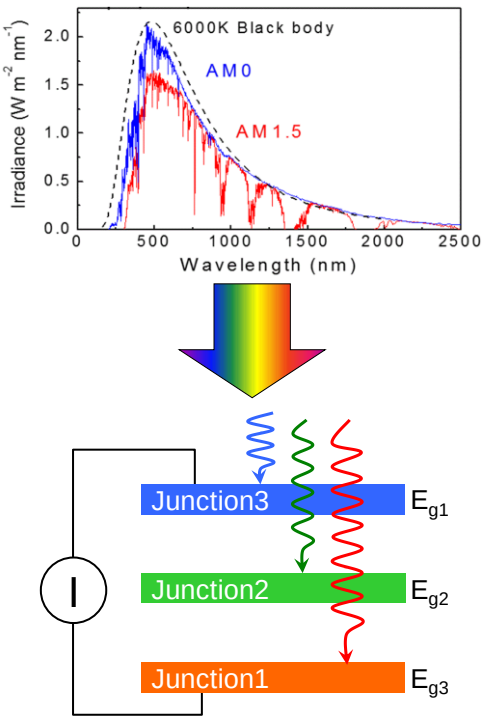

Figure 1.4 Example of full-spectrum solar cell

1.5 Transparent conducting oxide film

Transparent conducting oxide films (TCOs) are thin films of optically transparent and electrically conductive material. TCOs is one of the key components of a solar cell to collect charge carriers from the illuminated side of the cell. In order to increase a conversion efficiency of solar cells, it is required to utilize a wide range of photons in the solar spectrum. Therefore, several studied have been investigated on full spectrum solar cells including multi-junction solar cells (MJSCs) [18,19,20], intermediate band solar cells (IBSCs) [21.22.23], and so on. At present, a very high efficiency > 40% has been already achieved in MJSCs based on III-V semiconductors on a Ge bottom cell [20]. However, in those MJSCs, a TCO layer has not been used because of a lack of TCOs with a high transmittance in a wide spectral region from ultra-violet to infrared (IR)

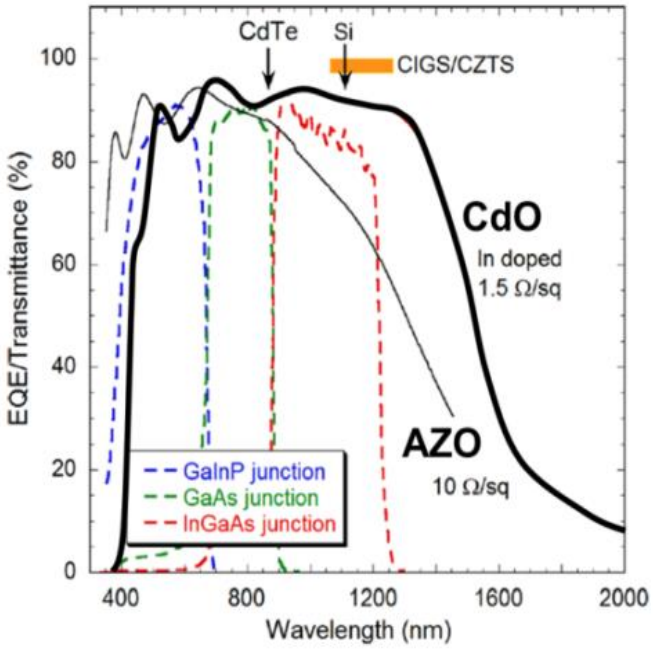

Figure 1.5 Transmittance spectra of a typical 300nm AZO films and an In-doped CdO TCO layer together with external quantum efficiency (EQE) of an inverted triple-junction (GaInP/GaAs/InGaAs) solar cell [29].

(~ from 300 to 1600 nm). The transmittance of widely used TCOs such as In_2O_3: Sn (ITO) [24], In_2O_3:Ga (IGO), and ZnO:Al (AZO) [25] have limited transmittance in the IR region (>1000 nm) because of their high electron concentration (> 10^{21} cm^{-3}) and low mobility (< 40 cm^2/Vs) which give rise to strong free carrier absorption (FCA) and plasma reflection [26,27,28]. Figure 1.5 shows the transmittance spectra of a typical 300nm AZO films and an In-doped CdO TCO layer together with external quantum efficiency (EQE) of an inverted triple-junction (GaInP/GaAs/InGaAs) solar cell [29]. Hence TCO materials with high transmittance extending into the IR region (> 1500 nm) [30] are essential for full solar spectrum photovoltaics. Among the various TCO materials, CdO has the highest reported mobility values of 200 cm^2/Vs at an electron concentration > 10^{21} cm^{-3} [28], and thus has been considered as a promising candidate for full spectrum solar cell applications [26,31,32,33,34,35]. Because of the high mobility, CdO is expected to realize a low resistive thin film with a low carrier concentration which can extend the FCA and a plasma reflection effects to

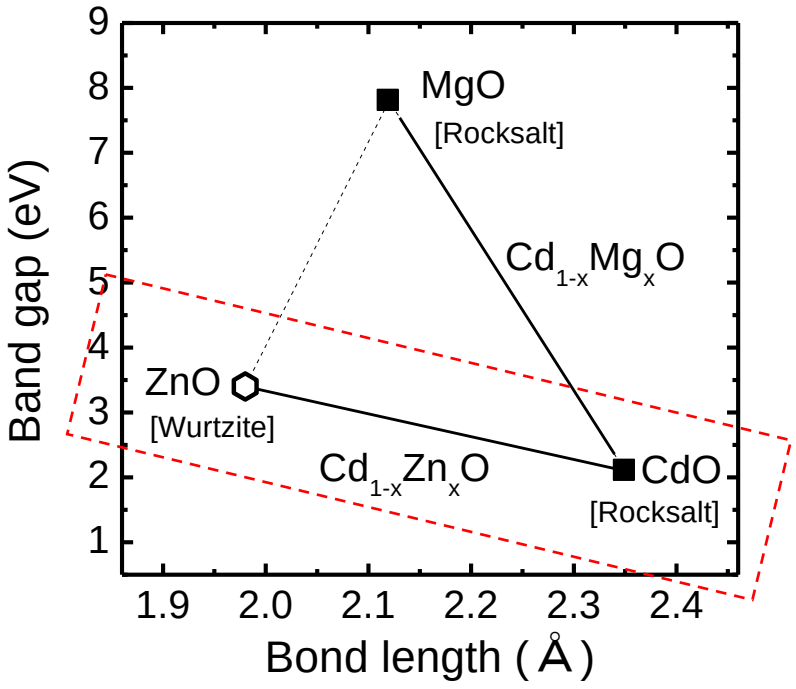

Figure 1.6 Band gap and structure of ZnO, CdO, and MgO. The structure of ZnCdO thin films has differed depending on the composition ratio of ZnO and CdO.

a much longer wavelength region (λ > 2000 nm) as shown in Fig.1.5. Hence it can be used as transparent conductors on devices in which transparency in the long wavelength infrared region is required [26,31].

However, as shown on Fig. 1.6 and Table 1, the band gap (2.3 eV) of CdO is small for a transparent conductor application. One of the ways to expand the band gap is alloying with a larger gap oxide such as ZnO which has a band gap of ~ 3.3 eV. However, because ZnO has a wurtzite (WZ) structure (α=3.25 Å, c=5.21 Å) whereas CdO a rocksalt (RS) structure (α=4.70 Å) as shown on Fig. 1.7 and Table 1.1, the crystal structure of $Zn_{1-x}Cd_xO$ (ZnCdO) is expected to change at a certain Cd composition.

Therefore, in study focuses on fabricating *n*-type ZnCdO thin films by MBE system under different conditions for following purpose.

Table 1.1 Fundamental physical properties of ZnO and CdO

	Crystal Structure	Lattice constant	band gap
ZnO	Wurtzite structure	a=3.250Å, c=5.207Å,	3.37eV
CdO	Rocksalt structure	a=4.670Å,	2.3eV

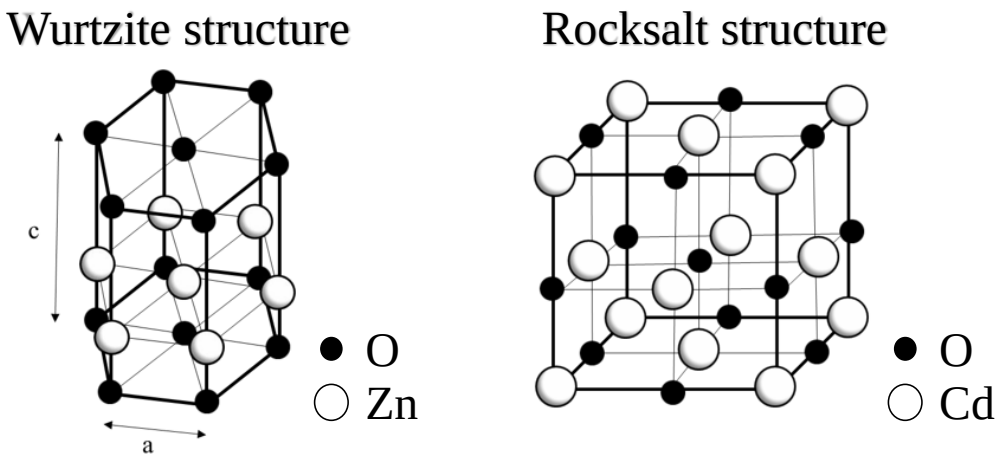

Figure 1.7 Structure of Wurtzite and Rocksalt of ZnO and CdO, respectively.

1.6 Purpose of this study

As described above, a full-spectrum solar cell requires a new TCO with high transmittance from infrared to ultraviolet to improve conversion efficiency. Among the various TCO material, CdO has taking excellent attention as promising material due to its good optical and electrical properties. Although, there are several reports on the synthesis of ZnCdO [31,36,37,38], only few studies reported the full range of $Zn_{1-x}Cd_xO$ by molecular beam epitaxy (MBE). This study focuses on fabricating *n*-type ZnCdO thin films by MBE system under different conditions for following purpose:

- To investigate the growth and characterization of ZnCdO thin films on α-Al_2O_3 (0001) substrates by MBE.
- To investigate the way to expand the band gap energy of ZnCdO thin films.
- To investigate the growth and characterization of ZnCdO thin films on MgO (100) substrates by MBE.
- To investigate the effect of Al doping on ZnCdO thin films on MgO (100) substrates by MBE.

In **Chapte**r 1, the introduction containing the background of the research, the history of a solar cell, the principle of a solar cell, current states of solar cells, introduction about transparent conducting oxide film is discussed.

In **Chapter 2**, experimental details and characterization methods of films are discussed. This study uses molecular beam epitaxy MBE for the films' growth. For the characterization

methods, reflection high-energy electron diffraction (RHEED), scanning electron microscope (SEM), X-ray Diffraction, energy dispersive X-ray spectroscopy (EDX), secondary ion mass spectroscopy (SIMS), ultraviolet-visible spectroscopy, and Hall effect measurements are used.

In **Chapter 3**, the growth and characterization of ZnCdO thin films on α-Al_2O_3 substrates are discussed. ZnCdO thin films are grown on α-Al_2O_3 substrates under the various Cd flux ratio (f_{Cd}= [Cd] / (Zn) + [Cd]) by MBE to grow a full range of $Zn_{1-x}Cd_xO$ compositions with various properties for a new type of TCO which have high transmittance in broad wavelength. The phase transition and corresponding optical and electrical properties of ZnCdO thin films are investigated. Results reveal that a higher optical band gap above 3.0 eV were archived on rocksalt ZnCdO thin films with high transmittance above 80 ~ 95 % in the visible range with a low resistivity of 5×10^{-4} Ωcm with a maximum mobility of ~ 90 cm^2/Vs and a high carrier concentration 4×10^{20} cm^{-3}.

Chapter 4 describes the effects of MgO (001) substrate on the structural, optical, and electrical properties of ZnCdO thin films. The α-Al_2O_3 substrates are replaced with MgO (001) substrates which have same rocksalt structure to archive a single crystalline RS-ZnCdO alloy with high Zn content. As the results, the optical band gap energy of ZnCdO increases and the largest optical band gap energy of 3.08 eV is obtained for x = 0.59 with an intrinsic band gap energy of 2.72 eV. RS-ZnCdO films show a low resistivity around 2.5×10^{-4} Ωcm with a maximum mobility of ~ 51.7 cm^2/Vs and a high carrier concentration around 5×10^{20} cm^{-3}.

Chapter 5 describes the effects of Al doping on the structural, electrical, and optical properties of ZnCdO thin films. Firstly, Al-doped ZnCdO thin films are grown on MgO (001) substrates under the various Al cell temperatures with fixed f_{Cd} to carry out the suitable Al doping. And then, the structural, optical, and electrical properties of Al-doped ZnCdO thin films are

investigated. As the results, the electron concentration increases higher than 10^{21} cm^{-3}, and a large optical band gap energy of 3.45 eV is observed in the RS-ZnCdO thin film having $x \approx 0.7$, with a resistivity of 1×10^{-4} Ω-cm, and a wide transmission window of up to 2000 nm.

And finally, **Chapter 6** summarizes the results obtained and concludes this thesis.

Reference

[1] S. E. Mousavi, H. Amini, P. Heydarpour, F. A. Chermahini, L. Godderis, “Air pollution, environmental chemicals, and smoking may trigger vitamin”, **122**, 2019, 67-90, DOI: 10.1016/j.envint.2018.11.052

[2] Andrew, Robbie; Peters, Glen (2021): “The Global Carbon Project’s fossil CO_2 emissions dataset”. figshare. Collection. https://doi.org/10.6084/m9.figshare.c.5646421.v1

[3] S. E. Mousavi, H. Amini, P. Heydarpour, F. A. Chermahini, L. Godderis, “Air pollution, environmental chemicals, and smoking may trigger vitamin D deficiency: Evidence and potential mechanisms”, Environment International, **122**, 2019, 67-90, https://doi.org/10.1016/j.envint.2018.11.052

[4] K. Philippopoulos, D. Deligiorgi, G. Karvounis, “Wind Speed Distribution Modeling in the Greater Area of Chania, Greece”, International Journal of Green Energy, **9**, (2012), 174-193, DOI: 10.1080/15435075.2011.622020

[5] "2014 Outlook: Let the Second Gold, Deutsche Bank Markets Research", https://www.dbresearch.com

[6] “World energy outlook 2019”. https://www.iea.org/topics/world-energy-outlook

[7] T. Khatib, A. Mohamed, K. Sopian, “A review of solar energy modeling techniques,” Renewable and Sustainable Energy Reviews, **16**, 2012, 2864-2869, https://doi.org/10.1016/j.rser.2012.01.064.

[8] J. Kreider, F. Kreith, "Solar energy handbook," New York: McGraw-Hil, 1981.

[9] National Renewable Energy Laboratory, NREL, USA, https://www.nrel.gov/pv/cell-efficiency.html

[10] G. Boyle, “Renewable Energy: Power for a Sustainable Future”, Oxford University Press, Oxford, 2004.

[11] K. W. Böer, “Survey of Semiconductor Physics”, John Wiley & Sons, New York, 2002.

[12] R. H. Bube, “Photovoltaic Materials”, London: Imperial College Press, 1998.

[13] J. R.Monkowski, J.Bloem, L. J.Giling, M. W. M.Graef, "Comparison of dopant incorporation into polycrystalline and monocrystalline silicon", Appl. Phys. Lett. **35 (5)**, 1979, 410–412, https://doi.org/10.1063/1.91143

[14] G. Hashmi, Md. A. R. Akand, M. K. Basher, M. Hoq, Md. H. Rahman., “Fabrication of Crystalline Silicon Solar Cell in Bangladesh: Limitations and Remedies,” International Journal of Scientific & Engineering Research, **7**, 2016, 581.

[15] M. K. DAS, N. S. CHICKERUR, "Fabrication of polycrystalline silicon solar cells showing high efficiency," Bull. Mater. Sci., **21**, 1998, 475-478.

[16] S. Mokkapati, C. Jagadish, " III-V compound SC for optoelectronic devices," Materials Today, **12(4)**, 2009, 22-32, https://doi.org/10.1016/S1369-7021(09)70110-5

[17] X. Deng, E. A. Schiff, “Amorphous Silicon–based Solar Cells,” University of Toledo, "Amorphous Silicon Based Solar Cells", in Handbook of Photovoltaic Science and Engineering, 2003, 505 - 565.

[18] S. R. Kurtz, K. A. Bertness, D. J. Friedman, A. E. Kibbler, C. Kramer, J. M. Olson, "in Proceedings of the 1st World Conference on Photovoltaic Energy Conversion", IEEE, New York, 1994, 2108–2111.

[19] P. K. Chiang, J. H. Ermer, W. T. Nishikawa, D. D. Krut, D. E. Joslin, J. W. Eldredge, B. T. Cavicchi, and J. M. Olson, "in Proceedings of the 25th IEEE Photovoltaic Specialists Conference", IEEE, New York, 1996, 183–186.

[20] R. R. King, D. C. Law, K. M. Edmondson, C. M. Fetzer, G. S. Kinsey, H. Yoon, R. A. Sherif, and N. H. Karam, "40% efficient metamorphic GaInP⁄GaInAs⁄Ge multijunction solar cells", Appl. Phys. Lett. **90**, 2007, 183516, https://doi.org/10.1063/1.2734507

[21] A. Luque and A. Martí, "Increasing the Efficiency of Ideal Solar Cells by Photon Induced Transitions at Intermediate Levels", Phy. Rev. Lett. **78**, 1997, 5014, https://doi.org/10.1103/PhysRevLett.78.5014

[22] Y. Okada, N. J. Ekins-Daukes, T. Kita, R. Tamaki, M. Yoshida, A. Pusch, et. Al, O. Hess, C. C. Phillips, D. J. Farrell, K. Yoshida, N. Ahsan, Y. Shoji, T. Sogabe, and J. –F. Guillemoles, "Intermediate band solar cells: Recent progress and future directions", Appl. Phys. Rev. **2**, 2015, 021302, https://doi.org/10.1063/1.4916561

[23] T. Tanaka, M. Miyabara, Y. Nagao, K. Saito, Q. Guo, M. Nishio, K. M. Yu, and W. Walukiewicz, "Photocurrent induced by two-photon excitation in ZnTeO intermediate band solar cells", Appl. Phys. Lett. **102**, 2013, 052111, https://doi.org/10.1063/1.4790643

[24] H.K. Yu and J. L. Lee, "Effect of ion beam assisted deposition on the growth of indium-tin-oxide (ITO) nanowires", CrystEngComm, **20**, 2014, 1-4, DOI https://doi.org/10.1039/C4CE00237G

[25] H. Kaneko, T. Togashi, T. Naka, M. Ishizaki, K. Kanaizuka, M. Sakamoto and M. Kurihana, "Low-Temperature Crystal Growth of Aluminium-Doped Zinc Oxide Nanoparticles in Melted Viscous Liquid of Alkylammonium Nitrates for Fabrication of Their Transparent Crystal Films", CrystEngComm, **46**, 2013, p.1-3, DOI: 10.1039/C4CE01336K

[26] D. S. Ginley, H. Hosono, D. C. Paine, "Handbook of Transparent Conductors", Springer, New York, 2011.

[27] Matthew D. McCluskey, Matthew D. McCluskey, Eugene E. Haller, Eugene E. Haller, "Dopants and Defects in Semiconductors", CRC Press, 2012, Chap. IX, https://doi.org/10.1201/b21986

[28] D. S. Ginley and J. D. Perkins, "in Handbook of Transparent Conductors", edited by D. S. Ginley, Springer Science Businesss, New York, 2010, Chap. I.

[29] Y. Chen, S. Zhang, W. Gao, F. Ke, J. Yan, B. Saha, C. Ko, J. Suh, B. Chen, J. W. Ager III, W. Walukiewicz, R. Jeanloz, and J. Wu, "Pressure-induced structural transition of $Cd_xZn_{1-x}O$ alloys", Appl. Phys. Lett. **108**, 2016, 152105, https://doi.org/10.1063/1.4947022

[30] K. M. Yu, M. A. Mayer. D. T. Speaks, H. He, R. Zhao, L. Hsu, S. S. Mao, E. E. Haller, W. Walukiewicz, "Ideal transparent conductors for full spectrum photovoltaics", J. Appl. Phys, **111**, 2012, 123505, https://doi.org/10.1063/1.4729563

[31] D. M. Detert, K. B. Tom, C. Battaglia, J. D. Denlinger, S. H. N. Lim, A. Javey, A. Anders, O. D. Dubon, K. M. Yu, W. Walukiewicz, "Crystal structure and properties of $Cd_xZn_{1-x}O$ alloys across the full composition range", Appl. Phys. Lett, **102**, 2013, 232103, https://doi.org/10.1063/1.4809950

[32] R. S. Mane, H. M. Pathan, C. D. Lokhande, Sung-Hwan Han, "An effective use of nanocrystalline CdO thin films in dye-sensitized solar cells", Solar Energy, **80**, 2006, 185, 10.1016/j.solener.2005.08.013

[33] S. Patil, S. Raut, R. Gore, B. Sankapal, "One-dimensional cadmium hydroxide nanowires towards electrochemical supercapacitor", New J. Chem., **39**, 2015, 9124, https://doi.org/10.1039/C5NJ02022K

[34] D. H. Fan, "Catalyst-free growth and crystal structures of CdO nanowires and nanotubes", J. Cryst. Growth, **311**, 2009, 2300, DOI: 10.1016/j.jcrysgro.2009.01.088

[35] S. Jambure, C. D. Lokhande, "Photoelectrochemical solar cells with chemically grown CdO rice grains on flexible stainless steel substrates", Mater. Lett. **106**, 2013, 133, 10.1016/j.matlet.2013.04.068

[36] D. M. Detert. K. B. Tom, C. Battaglia, J. D. Denlinger, S. H. N. Lim, A. Javey, A. Anders, O. D. Dubon, K. M. Yu, and W. Walukiewicz, "Fermi level stabilization and band edge energies in $Cd_xZn_{1-x}O$ alloys", J. Appl. Phys. **115**, 2014, 233708, https://doi.org/10.1063/1.4884683

[37] M. D. C. M. Tomas, A. H. Barbera. S. Agouram and V. M. Sanjose, "Induced crystallographic changes in $Cd_{1-x}Zn_xO$ films grown on r-sapphire by AP-MOCVD: the effects of the Zn content when $x \leq 0.5$", CrystEngComm, **22**, 2020, 74-78, https://doi.org/10.1039/C9CE01483G

[38] J. W. Min, S. Y. Bae, W. M. Kang, K. W. Park, E. K. Kang, B. J. Kim, D. S. Lee, Y. T. Lee, "Evolutionary Growth of Microscale Single Crystalline GaN on Amorphous Layer by Combination of MBE and MOCVD", CrystEngComm, **30**, 2015, 5849-5859, https://doi.org/10.1039/C5CE00543D

Chapter 2

Experimental details and characterization method of thin films

2.1. Substrate preparation

In this study, two types of substrates were used. For the first research, a c-plane α-Al_2O_3 (0001) substrate was used to grow ZnCdO to figure out the properties of ZnCdO thin films. And then, the substrate was changed from α-Al_2O_3 to MgO to improve the properties of the rocksalt-ZnCdO structure by using rocksalt structure substrate to reduce the lattice mismatch during the growth.

After cleaning, the substrates were set to the holder for MBE, and introduced to load lock chamber in the MBE system.

2.1.1. Cleaning method of α-Al_2O_3 (0001) substrate

The dust attached to the α- Al_2O_3 substrate was removed in methanol, and the surface dried with nitrogen gas blow. After that, ultrasonic cleaning was performed for 20 minutes in acetone and methanol, respectively, and then the surface was dried with nitrogen gas. For the etching to the surface of the substrate, the mixed solution was prepared from (sulfuric acid: phosphoric acid = 3: 1) and etched the sapphire substrate at a temperature of 80 ºC for 5 minutes.

2.1.2. Cleaning method of MgO substrate

The MgO substrate was cut appropriately 5mm × 5mm square size and blew with air blush to clean the surface. After that, ultrasonic cleaning was performed for 20 minutes in acetone and methanol, followed each with a nitrogen gun to blow off the liquid drop. For the MgO substrate, there was no specific etching process performed.

2.2 Film deposition

The deposition method is one of the keys to fabricating solar cells and TCOs. Depending on the deposition materials, the deposition method is divided into physical and chemical methods. Generally, sputtering [1,2], vapor deposition [3], sol-gel [4], solution growth [5], electron beam evaporation [6], thermal evaporation [7], electrodeposition [8], pulsed laser deposition [9], and molecular beam epitaxy (MBE) [10] are used as deposition method. In particular, MBE [11,12], MOCVD [13,14], sputtering [15,16], and PLD [17,18] methods are widely used as ZnCdO growth methods. In this research, MBE has been used for the deposition of ZnCdO thin films and the details of MBE is described as follows.

2.2.1 Molecular beam epitaxy (MBE).

Molecular Beam Epitaxy (MBE) is a method of growing a thin film by epitaxial growth by evaporating the element into a vaporized molecular beam by heating a raw material such as metal in an ultra-high vacuum [18]. Among the component elements that reach the substrate in the beam

shape, molecules that cannot grow on the substrate are excluded from the growth process by the vacuum system, and only the "fresh" molecular beam from the evaporation source reaches the substrate surface. This method is performed in ultra-high vacuum pressure about 10^{-8} Pa. Moreover, the number of molecules of each element reaching the substrate is uniquely determined by the geometry of the vapor deposition system and the evaporation source. Therefore, it is possible to accurately control the crystal growth rate, the ratio of the impurity concentration, or the mixing ratio. In addition, oxygen or hydrogen can be produced by using a radical gun. The surface can be observed during crystal growth using a reflection high-energy electron diffraction.

- Advantages of MBE
  - MBE is a low-temperature process.
  - MBE process can be used for generating detailed doping profiles as it regulates the amount of dopant.
  - As the MBE process is based on evaporation, no chemical reactions are involved.
  - For the MBE process, safety precautions are not required extensively as compared to those required in a CVD process.
- Disadvantages of MBE
  - For the overall perfect and pure film, it is necessary to maintain a very low pressure of the order of 10^{-8} Pa.
  - This process is very expensive as compared to the sputtering or CVD process.
  - The growth rate in the MBE process is 0.01 – 0.3 μm/min, which is very small compared to the other deposition method.

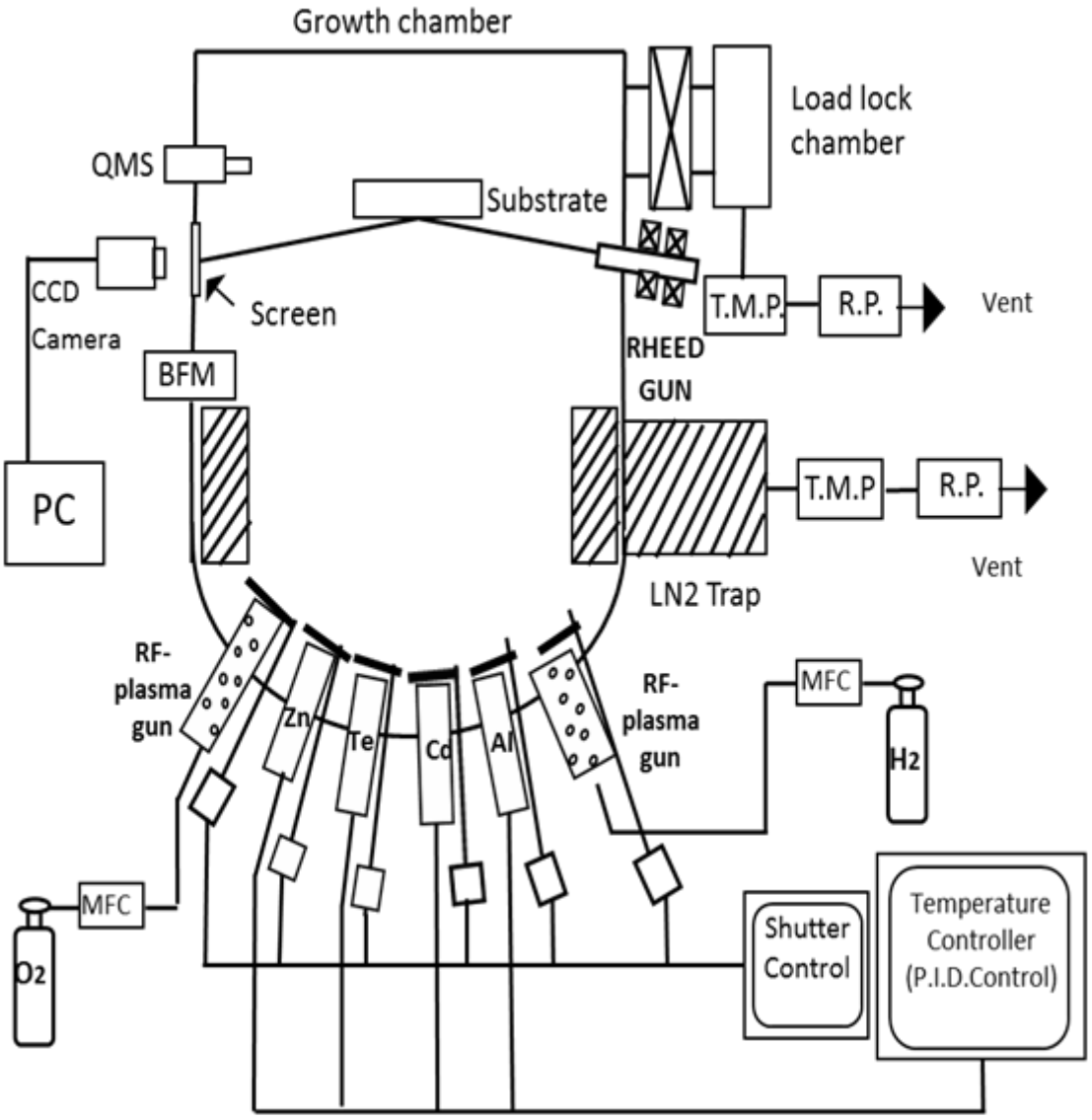

Figure 2.1 Schematic of molecular beam epitaxy system.

2.3. Characterization method

In this section, the material characterization methods used to analyze the surface morphology, crystal structure, composition, optical properties of transmittance and reflectance, thickness, and electrical properties of conductivity, mobility, carrier type and concentration of the deposited films are represented.

2.3.1 Reflection high-energy electron diffraction (RHEED)

Reflection high-energy electron diffraction (RHEED) is a technique in which an electron beam of about 10 keV ~50 keV is incident on a surface of a sample at a shallow incident angle, an electron beam diffracted by a crystal lattice is projected onto a fluorescent screen and observe the appearance of the crystal surface. Since the angle of incidence is shallow, the electron beam penetrates only a few atomic layers from the sample's surface and is highly sensitive to the surface lattice structure because of its significant diffraction from the surface.

RHEED has a great feature that can be observed without disturbing growth. This feature makes it widely known that RHEED is an excellent way to investigate surface structures in many areas. Figure 2.2 shows the relationship between the shape of the substrate surface and the RHEED pattern.

As shown in Fig. 2.2. (a), if the substrate's surface is roughened, a diffraction pattern of a spot shape due to the transmitted electron beam is observed. When growth starts on such a roughened substrate, a soft surface, as shown in Fig. 2.2. (b), becomes difficult to transmit the

electron beam, and a long-dotted stripe pattern is produced. As the growth continues, the thin film grows flat, but there are countless atomic layer steps on its surface, as shown in Fig. 2.2.(c). Therefore, the point of intersection with Ewald's sphere in the vicinity of the 0th Laue zone became a line and was observed as a linear strike pattern according to the growth of the thin film. However, in the case of a completely flat surface, as shown in Fig. 2.2. (d), the RHEED pattern becomes a short-dashed line [19].

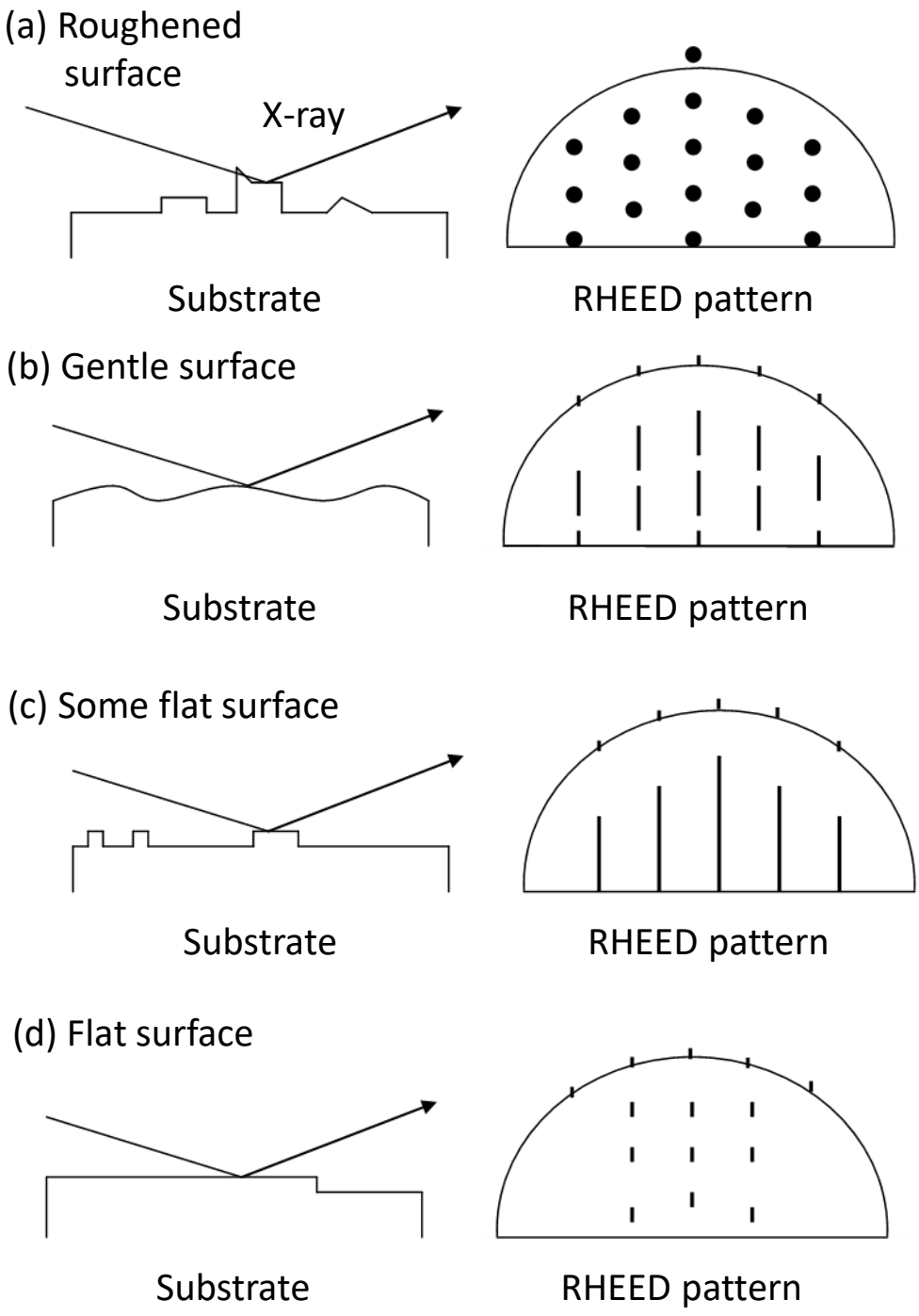

Figure 2.2 Relationship between the shape of the substrate surface and RHEED pattern.

2.3.2 X-ray diffraction (XRD)

X-ray diffraction (XRD) is an X-ray-based method for determining the crystal structure of a material. It was discovered by Max von Laue in 1912 in Germany. The XRD peak is obtained by detecting the reflected intensities and scattering angles of the X-rays that leave the material. X-ray is irradiated by the X-ray tube as shown in Fig. 2.3, and Bragg's law and diffraction used to explain the working principle of XRD in Fig. 2.4.

At here, $n\lambda = \overline{BC} + \overline{CD}$.

$\overline{BC} = \overline{CD} = d \sin\theta$.

Therefore, $\overline{BC} + \overline{CD} = 2d \sin\theta$.

$n\lambda = 2d \sin\theta$.

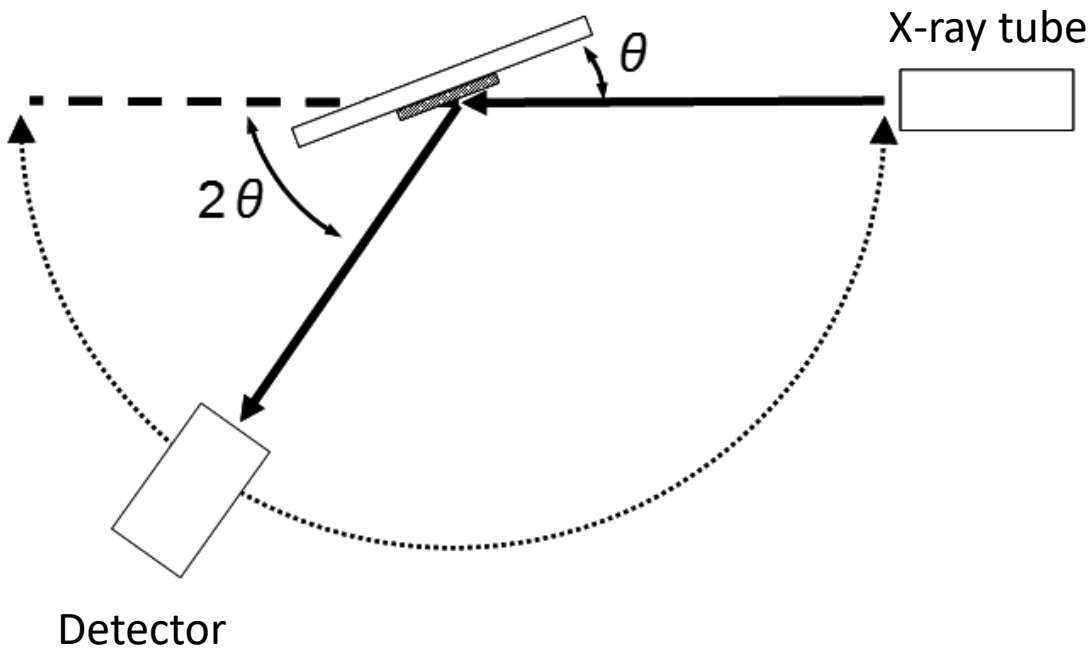

Figure 2.3 Schematic of XRD.

Also, lattice constants can be calculated by following equation for cubic crystalline：

$$\frac{1}{d_{hkl}^2} = \frac{h^2+k^2+l^2}{\alpha^2}.$$

In this study, PANalytical X'Pert MRD (Materials Research X-ray Diffraction) system is used.

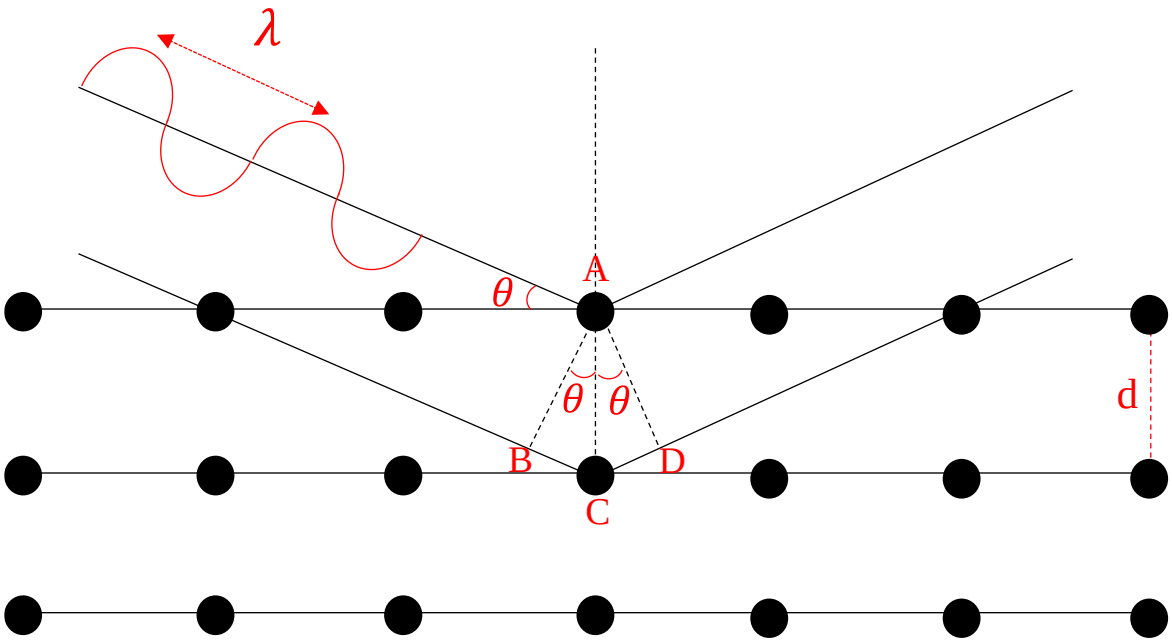

Figure 2.4 Schematic of XRD.

2.3.3. Energy dispersive X-ray spectroscopy (EDX)

In this study, the system named Philips XL30 EEG SEM are used. When one type of light, such as an electron beam or an X-ray, is projected onto an object, the electrons in the electron shell are struck out. At this time, the electrons in the outer shell find stability and move to a lower potential energy cabinet. The extra energy generated by this transition is radiated to the outside, which is called characteristic X-rays or fluorescent X-rays. The X-rays come out in different energy and intensity depending on atoms. EDX (Energy Dispersive X-ray spectroscopy) is an analytical method in which an energy dispersion detector detects an X-ray, and the element and concentration constituting the object are examined from the energy.

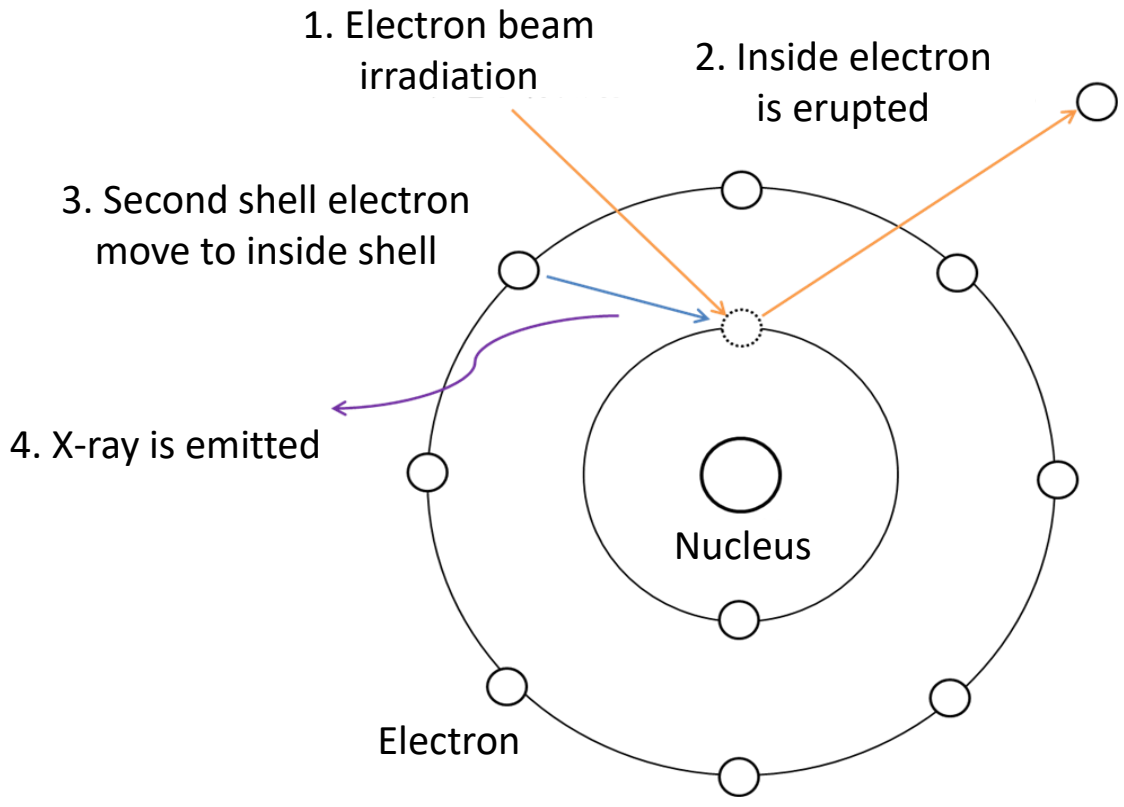

Figure 2.5 Principle of EDX

2.3.4 Transmittance and reflectance measurements

The transmittance and reflectance spectra of the films are measured using a Jasco V-570. Spectrophotometers include ultraviolet, visible, near infrared, and infrared rays depending on the wavelength range measured.

In this study, we used the double-beam method, which directly measures the reference and control samples, with the wavelength range is between 300 ~ 2500 nm with a wavelength accuracy of 1.5 nm.

Figure 2.6 is a schematic diagram of the process of the spectrophotometer. The light from the light source is condensed and enters the monochromator. This light is diffracted by the monochromator and is condensed on the exit slit. The light coming out of the exit slit becomes monochromatic light.

The monochromatic light is divided into two beams by a sector mirror, one side to the measurement sample and the other to the control sample. The light passing through the sample or

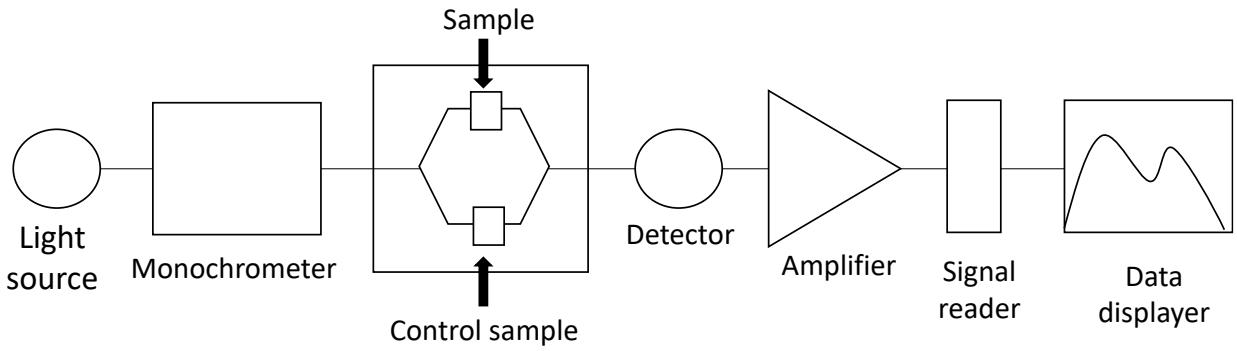

Figure 2.6 Schematic diagram of the process of the spectrophotometer

control sample is incident on the amplifier or PbS photoconductive cell and then is digitized by the spectrometer and the software program.

With the results of transmittance and reflectance, the optical absorption coefficient (α) of thin film was obtained by using the following equation :

$$\alpha = -\frac{1}{d}\ln\frac{-(1-R)^2 - \sqrt{(1-R)^4 + 4T^2R^2}}{2TR^2} \qquad (2.1)$$

where α is the absorption coefficient, *d* is the thickness of the thin film, *R* is the reflectance of, and *T* is the transmittance of thin film.

In a direct transition semiconductor, the relationship between the optical absorption coefficient α and the incident photon energy hν can be expressed by the following equation :

$$\alpha = A(h\nu - E_g)^{\frac{1}{2}} \qquad (2.2)$$

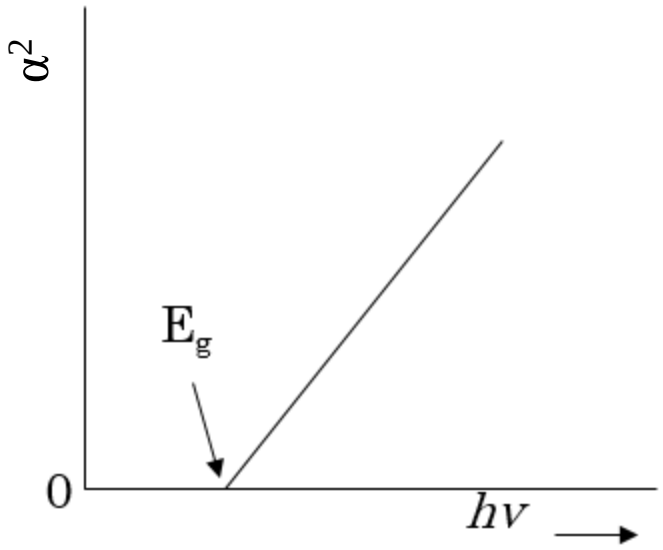

Figure 2.7. Example plot of α^2 vs photon energy.

Here, E_g is the band gap energy, and A is the proportionality constant. Therefore, as shown in Fig. 2.7, the band gap energy can be obtained by plotting the square of the optical absorption coefficient α against photon energy hν and extrapolating the linear portion of α^2 on the horizontal axis.

2.3.5. Surface step profiler

This instrument measures the thickness of the sample by directly contacting the needle on the sample surface. The needle is moved horizontally in the contact state, moving up and down according to the surface. An induced electromotive force is generated in the secondary coil by the movement of the needle, and a differential transformer amplifies the voltage, and the difference of

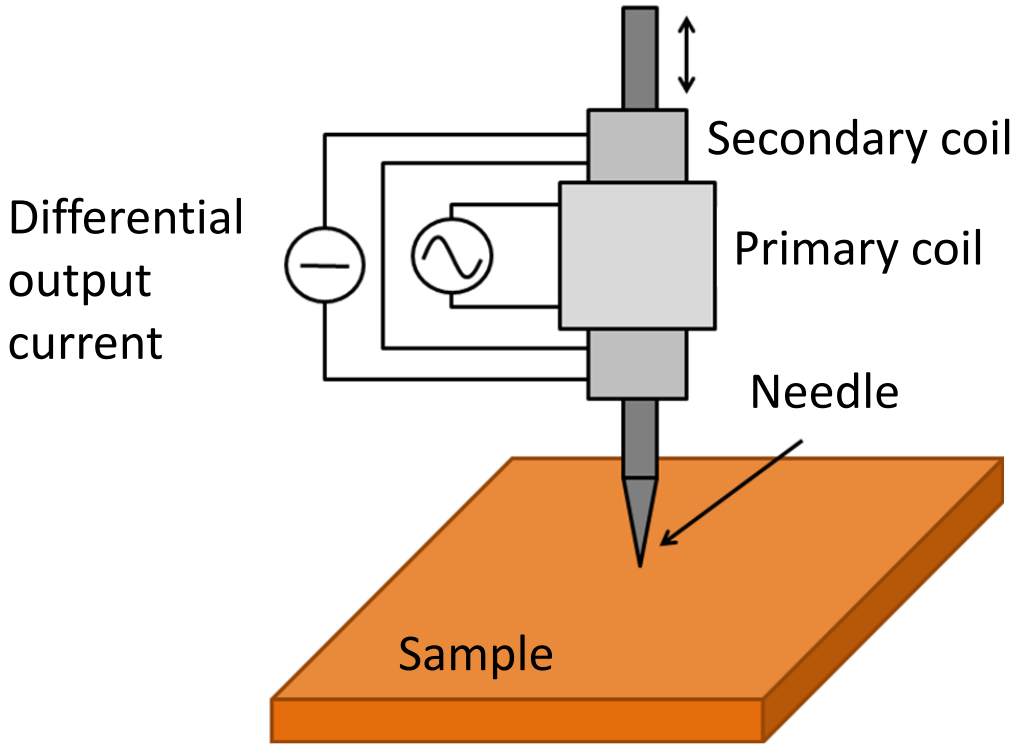

Figure 2.8 Schematic diagram of surface step profiler.

the surface of the sample can be measured in the unit of the nanometer. Figure 2. 8 shows the schematic of the surface step profiler.

2.3.6. Hall effect measurement

Hall effect measurements (Resitest 8300) used to measure the conduction type, resistivity, carrier concentration and mobility of thin films by using the van der Pauw method at room temperature. This method is suitable for a thin film or thin semiconductor such as an epitaxial layer.

The Hall effect is owing to the nature of the current in a conductor which is composed of the movement of many small charge carriers like electrons and holes. When a magnetic field is applied to the films, these charges experienced a force, termed as the Lorentz force. Due to the magnetic field, electrons and holes will be deflected in opposite directions. The separation of charge established an electric filed that opposes Lorentz force. In the meantime, a steady electrical potential is established as long as the charge is starting to flow.

2.3.7 Vacuum deposition

Vacuum deposition is one of the methods used when a metal is deposited on the surface of a sample, such as a substrate under a vacuum of about 10^{-3} to 10^{-5} Pa. Mo or other high-melting-point metal plates are set to the two heating devices and put the material to be deposited on it. Thereafter, the raw material is melted and evaporated by flowing a large current of about 50A and

heating. The evaporated raw material is deposited on the surface of the substrate to produce a thin film. A schematic diagram of a typical vacuum deposition system is shown in Fig. 2.9.

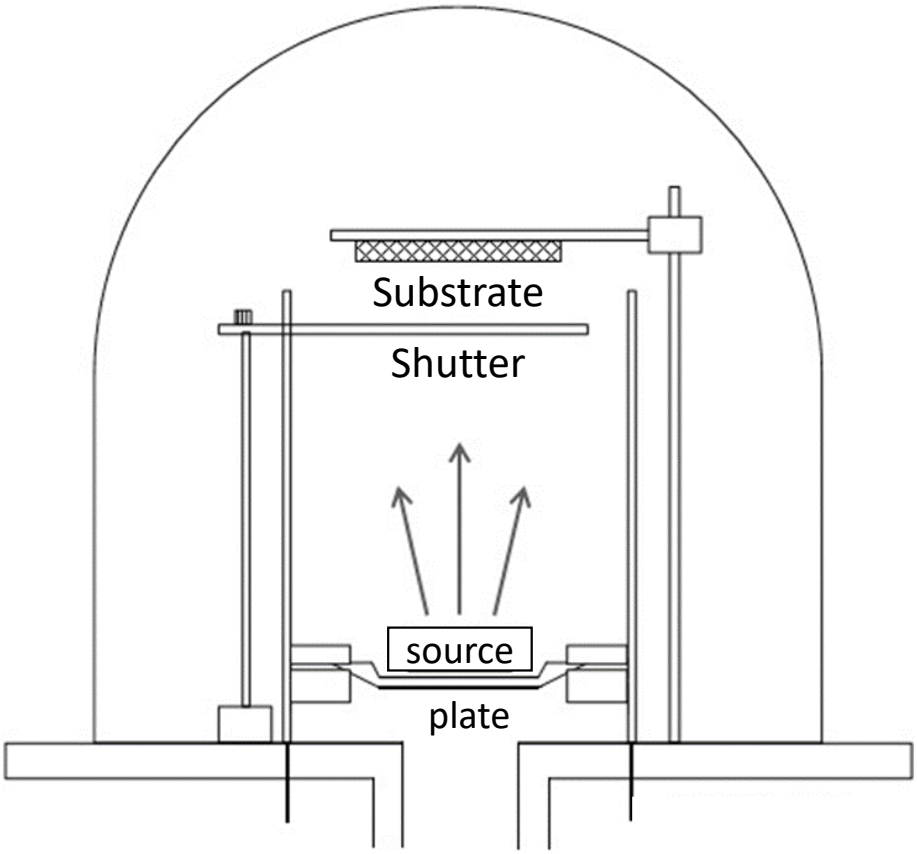

Figure 2.9. Schematic of Vacuum Deposition.

Reference

[1] A. A. Ogwu, E. Bouquerel, et al, “The influence of rf power and oxygen flow rate during deposition on the optical transmittance of copper oxide thin films prepared by reactive magnetron sputtering” Appl. Phys., **38**, 2005, 266-271, https://doi.org/10.1088/0022-3727/38/2/011

[2] A. Parretta, M. K. Jayaraj, A. D. Nocera, S. Loreti, L. Quercia, A. Agati, “Electrical and Optical Properties of Copper Oxide Films Prepared by Reactive RF Magnetron Sputtering”, Phys. Status Solidi A, **155**, 1996, 399- 404, https://doi.org/10.1002/pssa.2211550213

[3] T. Maruyama, Jpn. “Copper Oxide Thin Films Prepared from Copper Dipivaloylmethanate and Oxygen by Chemical Vapor Deposition”, J. Appl. Phys., **37**, 1998, 4099-4102, https://doi.org/10.1143/JJAP.37.4099

[4] L. Arnelao, D. Barreca, M. Bertapelle, G. Bottaro, C. Sada, E. Tandello, “A sol–gel approach to nanophasic copper oxide thin films”, Thin Solid Films, **442**, 2003, 48-52, https://doi.org/10.1016/S0040-6090(03)00940-4

[5] M. Yang, J. J. Zhu, “Spherical hollow assembly composed of Cu_2O nanoparticles”, J. Cryst. Growth, **256**, 2003, 134-138, https://doi.org/10.1016/S0022-0248(03)01298-3

[6] V. Figueiredo, E. Elangovan, G. Goncalves, et al, “Electrical, structural and optical characterization of copper oxide thin films as a function of post annealing temperature”, J. Phys. Status Solidi A, **206**, No. 9, 2009, 2143–2148, https://doi.org/10.1002/pssa.200881797

[7] L. S. Huang, S. G. Yang, T. Li, B. X. Yu, Y. W. Du, et al, “Preparation of large-scale cupric oxide nanowires by thermal evaporation method”, Cryst. Growth, **260**, 2004, 130-135, https://doi.org/10.1016/j.jcrysgro.2003.08.012

[8] Y. C. Zhou, J. A. Switzer, “Galvanostatic electrodeposition and microstructure of copper (I) oxide film”, Mater. Res. Innov., **2**, 1998, 22-27, https://doi.org/10.1007/s100190050056

[9] N. Kikuchi, K. Tanooka, “Electrical and structural properties of Ni-doped Cu_2O films prepared by pulsed laser deposition”, Thin Solid Films, **486**, 2005, 33-37, DOI:10.1557/JMR.1994.1280

[10] R. Kita, K. Kawaguchi, T. Hase, T. Koga, R. Itti, T. Morishita, “Effects of oxygen ion energy on the growth of CuO films by molecular beam epitaxy using mass-separated low-energy O^+ beams”, J. Mater. Res., **9**, 1994, 1280-1283. https://doi.org/10.1557/JMR.1994.1280

[11] X.J. Wang, I.A. Buyanova, W.M. Chen, M. Izadifard, S. Rawal, D.P. Norton, S.J. Pearton, A. Osinsky, J.W. Dong, A. Dabiran, “Band gap properties of $Zn_{1-x}Cd_xO$ alloys grown by molecular-beam epitaxy”, Appl. Phys. Lett., **89**, 2006, 151909, https://doi.org/10.1063/1.2361081

[12] K. Sakurai, T. Kubo, D. Kajita, T. Tanabe, H. Takasu, S. Fujita, S. Fujita, “Blue Photoluminescence from ZnCdO Films Grown by Molecular Beam Epitaxy”, J. Appl. Phys., **39** 2000, L1146, https://iopscience.iop.org/article/10.1143/JJAP.39.L1146/pdf

[13] F. Bertram, S. Giemsch, D. Forster, J. Christen, R. Kling, C. Kirchner, A. Waag, “Optical and structural analysis of ZnCdO layers grown by metalorganic vapor-phase epitaxy”, Appl. Phys. Lett., **88**, 2006, 061915, https://doi.org/10.1063/1.1620674

[14] Th Gruber, C. Kirchner, R. Kling, F. Reuss, A. Waag, F. Bertram, D. Forster, J. Christen, M. Schreck, “Optical and structural analysis of ZnCdO layers grown by metalorganic vapor-phase epitaxy”, Appl. Phys. Lett., **83**, 2003, 3290, https://doi.org/10.1063/1.1620674

[15] I. Shtepliuk, V. Khranovskyy, G. Lashkarev, V. Khomyak, A. Ievtushenko, V. Tkach, V. Lazorenko, I. Timofeeva, R. Yakimova, “Microstructure and luminescence dynamics of ZnCdO films with high Cd content deposited on different substrates by DC magnetron sputtering method”, Applied Surface Science, **276**, 2013, 550-557, https://doi.org/10.1016/j.apsusc.2013.03.132

[16] Y.R. Sui, Y.G. Yue, Y. Cao, B. Yao, X.Y. Liu, J.H. Lang, M. Gao, X.F. Li, X.Y. Li, J.H. Yang, “Influence of substrate temperature on structural and optical properties of ZnCdO thin films deposited by dc magnetron sputtering”, Ceramics International, **40(7)**, 2014, 9189-9194, https://doi.org/10.1016/j.ceramint.2014.01.136

[17] M. Lange, C.P. Dietrich, G. Benndorf, M. Lorenz, J. Zuniga-Perez, M. Grundmann, “Thermal stability of ZnO/ZnCdO/ZnO double heterostructures grown by pulsed laser deposition”, J. Cryst. Growth, **328**, 2011, 13, DOI: 10.1016/j.jcrysgro.2011.06.030

[18] J. Jiang, L.P. Zhu, H.P. He, Y. Li, Y.M. Guo, L. Cao, Y.G. Li, K.W. Wu, L.Q. Zhang, Z.Z. Ye, “Structural and optical properties of ZnCdO/ZnO multiple quantum wells grown on sapphire substrates using pulsed laser deposition”, J. Appl. Phys., **112**, 2012, 083513, https://doi.org/10.1063/1.4759325

[19] K. M. Yu, A. Marie , Mayer, T. Derrick, H.i He, R. Zhao, L. Hsu, S. Samuel, S. Mao, E. E. Haller, W. Walukiewicz, “Ideal Transparent Conductors for Full Spectrum Photovoltaics,” J. Appl. Phys. **111**, 2012, 123505, https://doi.org/10.1063/1.4729563

Chapter 3

Realization of RS-$Zn_{1-x}Cd_xO$ thin films with optical band gap above 3.0 eV by molecular beam epitaxy

3.1 Introduction

As explained in **Chapter 1**, TCOs is one of the key components of a solar cell to collect charge carriers from the illuminated side of the cell. In order to increase a conversion efficiency of solar cells, it is required to utilize a wide range of photons in the solar spectrum. So far, there are several reports on the synthesis of ZnCdO [1,2,3,4]. Detert et al. deposited ZnCdO films on soda lime glass substrates using a pulsed filtered cathodic arc deposition method and reported that the phase transition occurred at $x \sim 0.7$ and the largest band gap of RS-ZnCdO with $x \sim 0.7$ is 2.8 eV [1]. On the other hand, the band gap of the WZ-ZnCdO decreased with increasing Cd down to a value of ~ 1.7 eV at the phase transition point of $x \sim 0.7$. Using a non-equilibrium growth technique such as MBE [5], which can grow high-quality thin films at low temperature, the RS to WZ phase transition may be extended to a lower Cd composition, leading to further increase of the band energy.

In this **Chapter 3**, growth of ZnCdO thin films with a wide range of Cd composition on α-Al_2O_3 (0001) substrates by MBE are reported. The phase transition and corresponding optical and electrical properties of ZnCdO thin films are investigates in detail.

3.2 Experimental

ZnCdO thin films were grown on α-Al_2O_3 (0001) substrates by a conventional MBE system with a radio frequency (RF) radical cell. The background pressure of the growth chamber is less than 6×10^{-8} Pa. Zn (7N) and Cd (6N) were used as source materials. The α-Al_2O_3 (0001) substrates were ultrasonically cleaned in organic solvents. The flow rate of oxygen was kept constant at 0.3 sccm, and the RF power was set to 300 W. after introducing α-Al_2O_3 (0001) substrates into the growth chamber, firstly, the substrate temperature was changed from 100 to 250°C with the Cd flux ratio f_{Cd} (= [Cd] / ([Zn] + [Cd])) = 0.90 to find out the suitable growth temperature for ZnCdO thin film. Cd flux fixed at 1.2×10^{-4} Pa, and Zn flux differed depending on Cd flux. After optimizing the growth temperature, the Cd flux ration f_{Cd} was varied between 0.85 and 1 to grow the full range of Cd composition at 250°C substrate temperature.

During the growth, a reflection high-energy electron diffraction (RHEED) pattern was recorded to monitor the film structure. After the growth, the film thickness was measured using a surface step profiler. The composition of ZnCdO was measured by energy dispersive X-ray spectroscopy (EDX) and Rutherford backscattering spectrometry (RBS) using a 3.04 MeV He^{++} beam. Crystal structures of the films were examined by conventional θ-2θ X-ray diffraction (XRD) using a Cu Kα radiation. The transmittance and reflectance were measured using a double-beam spectrophotometer in the wavelength range of 200 ~ 2000 nm. The band gap energy of the films was determined by a square plot of absorption coefficient (α) obtained from the transmittance and reflectance. The electrical properties were measured by Hall effect measurement using the Van der Pauw configuration with In as ohmic contact at room temperature.

3.3 Results and discussion

3.3.1 Effects of substrate temperature

Figure 3.1 shows photographs of $Zn_{1-x}C_xdO$ thin film grown with f_{Cd} = 0.9 at the temperature range of 100 ~ 250°C. Relatively thick black films with thicknesses over 1μm were obtained when the substrate temperature was lower than 200°C. However, at the substrate temperature of 250°C, a yellowish thin film with about 60 nm thickness was obtained. This result suggests that at a growth temperature lower than 250°C, the substrate does not provide sufficient thermal energy for the metal atoms to react with the O.

Figure 3.2 shows the XRD patterns of ZnCdO thin films grown on α-Al_2O_3 (0001) substrates at different substrate temperatures. When grown with substrate temperature lower than 200°C, broad diffraction peaks corresponding to metallic Cd at 32°, 34.8° and 38.2° with low

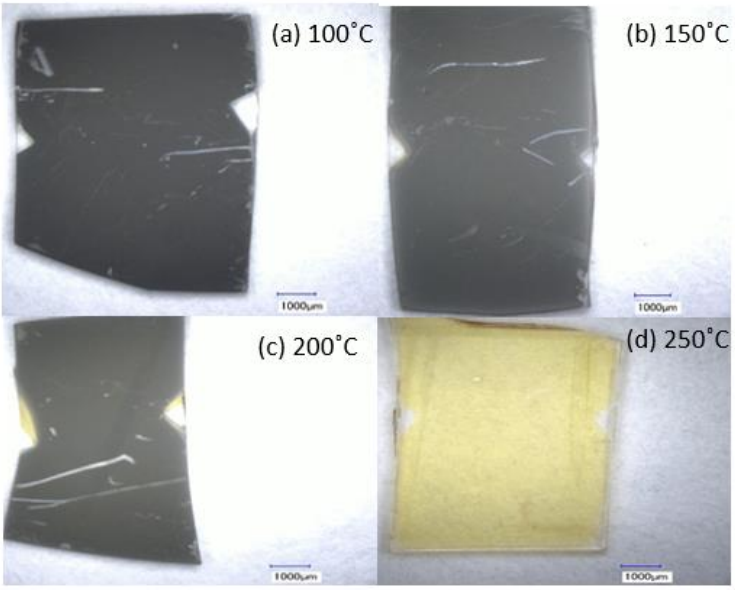

Figure 3.1 Photographs of ZnCdO thin films grown on α-Al_2O_3 (0001) substrates at various substrate temperatures.

intensity are observed, indicating the presence of unreacted Cd and that these films are amorphous or nanocrystalline. With increasing substrate temperature, the intensity of the diffraction peak between 33° ~ 34° increased. This peak is located in between the diffraction peaks from RS-CdO (111) and WZ-ZnO (0002), and can be assigned as WZ-ZnCdO (0002) as discussed later. A strong ZnCdO peak is detected from the film grown at 250°C, indicating that with a high substrate temperature of 250°C ZnCdO films with good crystallinity are obtained. Effects of the substrate temperature on the crystallinity has also been reported for sputtered ZnCdO films [6] and the reported results are consistent with our present work by MBE growth. The average grain size of the film grown at 250°C can be estimated to be ~ 16 nm from the width of the diffraction peak. Note also that as the substrate temperature increases, the WZ-ZnCdO peak shifted gradually to

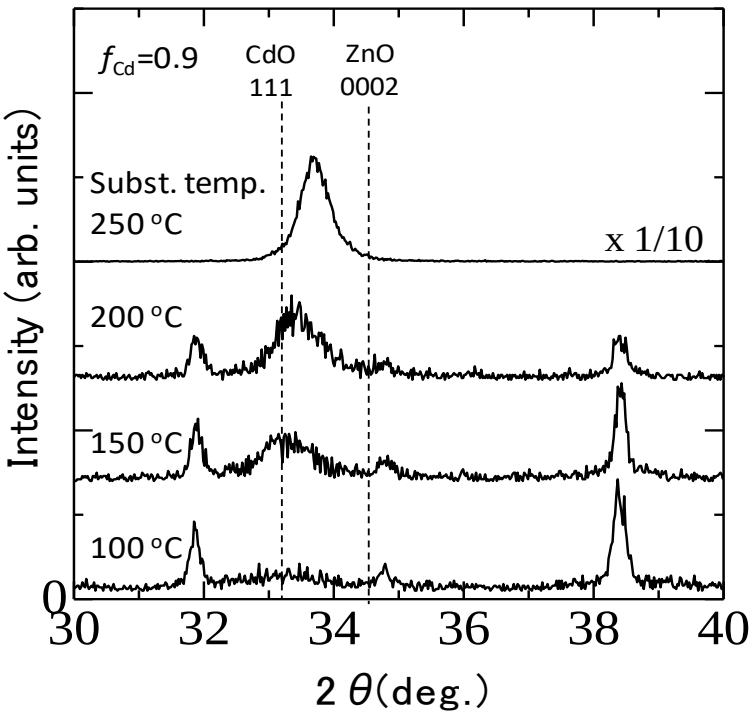

Figure 3.2 XRD patterns of ZnCdO thin films grown on α-Al_2O_3 (0001) substrates at different substrate temperature.

higher angle. Since the ionic radius of Cd^{2+} (109 pm) is significantly larger than that of Zn^{2+} (88 pm), this suggest that less Cd is incorporated in the alloy at higher growth temperature. These results suggest that with our MBE growth condition, in order to grow crystalline ZnCdO thin films were grown at 250°C under different Cd flux ratios to investigate the effect of Cd flux ratio on the properties of ZnCdO films.

3.3.2 Effects of Cd flux ratio on the properties of ZnCdO films.

Figure 3.3 shows the Cd content determined by EDX analyses in ZnCdO thin films on α-Al_2O_3 (0001) substrates under different Cd flux ratios. The Cd content in the film is below the

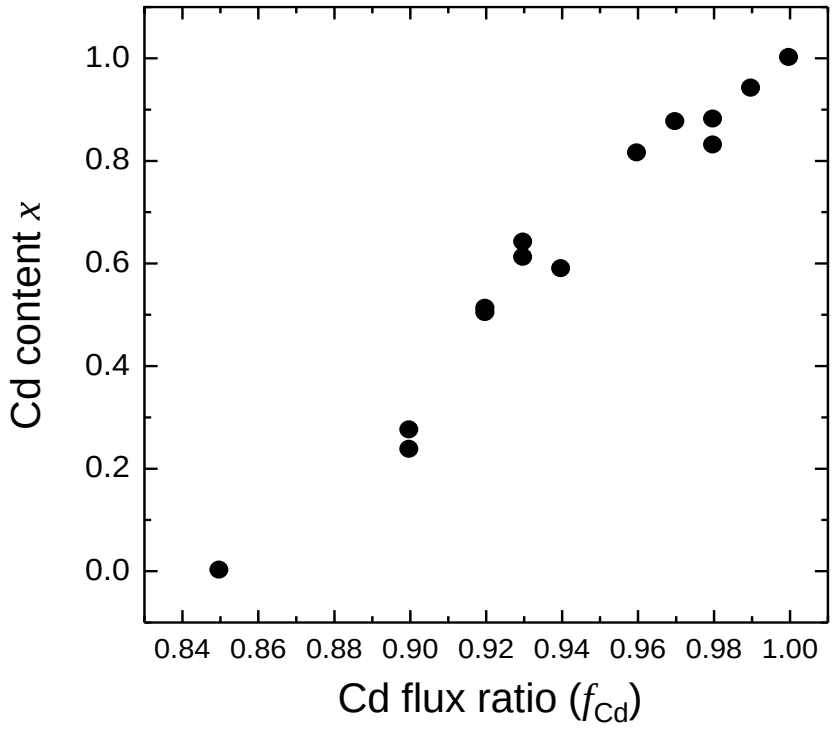

Figure 3.3 Cd content *x* in ZnCdO thin films grown on α-Al_2O_3 (0001) substrates under various Cd flux ratios as measured by EDX

detection limit of EDX (< 1%), and it is considered the film is pure ZnO with $x = 0$. As the f_{Cd} increases, the Cd content x in $Zn_{1-x}CxdO$ thin films increases gradually up to 1. Thus, ZnCdO films with different composition can be grown by controlling the Cd ratio.

Figure 3.4 shows XRD patterns of ZnCdO films grown at 250°C with the different Cd content x. all the films are polycrystalline with a thickness of around 60 nm. In the ZnO film with x=0 grown at $f_{Cd} = 0.85$, only the peak 34.4° corresponding to WZ-ZnO (0002) diffraction is observed. With increasing Cd content, this diffraction peak shifted to lower angle suggesting a larger lattice parameter. This is consistent with the incorporation of more Cd with a larger ionic radius in the Zn sub lattice in WZ-ZnCdO [7]. On the other hand, at the Cd content x=1, only the RS-CdO (111) diffraction peak at 33° is observed. With decreasing Cd content from 1 to 0.75 this RS (111) diffraction peak shifts toward higher 2θ due to the replacement of Cd by Zn. In ZnCdO films deposited on soda-lime glass substrates, a RS-ZnCdO (200) peak was also observed at around 38 ~ 39° [1,7] although it was not detected clearly in this study. Since on α-Al_2O_3 (0001) was used as substrates in this study, the RS-ZnCdO is expected to have a (111) preferred orientation. Note that for samples with Cd content $x = 0.51$ and 0.62, the diffraction peak becomes very weak and broad. It has been reported previously that the composition region where both RS and WZ phases co-exist depends on the growth method and lies in the range of $x \sim 0.4$ to 0.7 [1,7,8]. Therefore, the broad weak diffraction for ZnCdO film with $0.51 < x < 0.62$ may correspond samples with a

mixed phase of WZ and RS. At the Cd content x = 0.51, mixed peak from RS-ZnCdO (x=0.61) and WZ-ZnCdO (x=0.06) are observed by 2 peak fitting as red-dashed line.

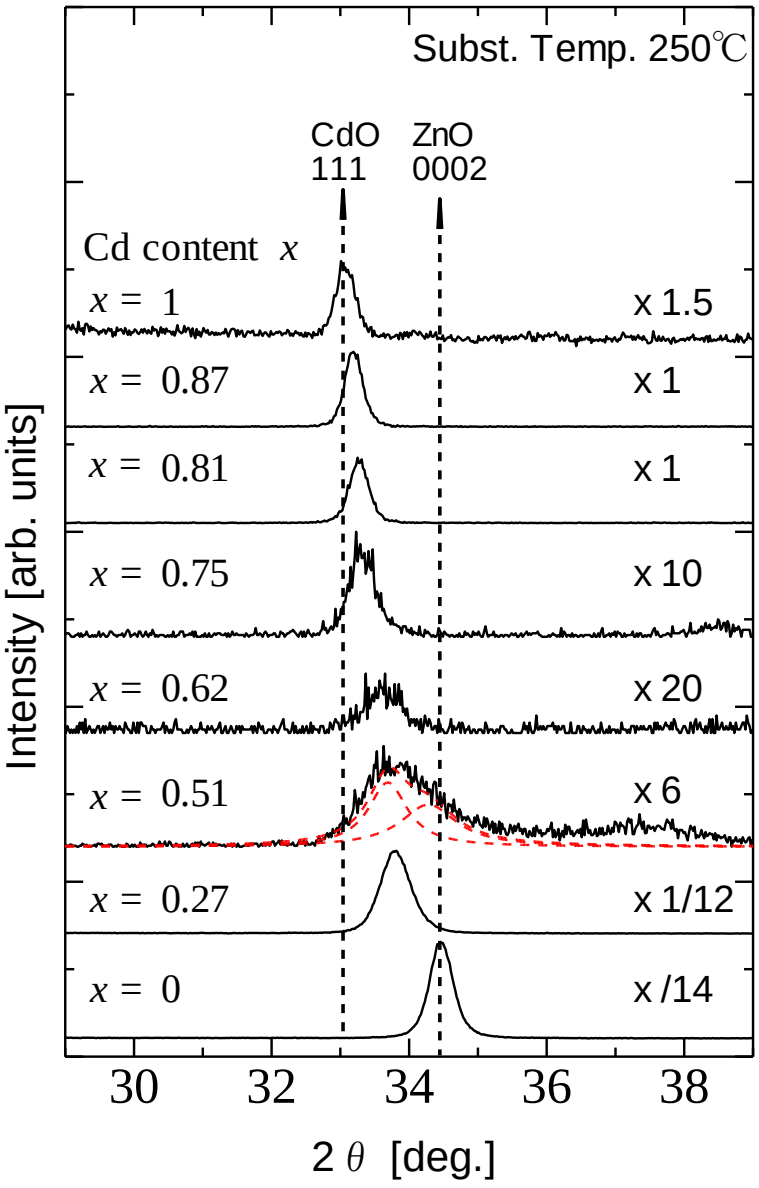

Figure 3.4 XRD patterns of ZnCdO thin films grown on α-Al_2O_3 (0001) substrate under various Cd flux ratios.

In order to investigate the optical properties of ZnCdO thin films, transmittance and reflectance spectra of ZnCdO thin films were measured by a double-beam spectrophotometer in the wavelength range of 200 ~ 2000 nm, and the absorption coefficients were calculated using the Beer-Lambert Law. The absorption spectra for $x \leq 0.5$ and $x \geq 0.58$ were plotted separately in Fig. 3. 5(a) and (b), respectively.

In Fig. 3. 5(a), the absorption edge energy gradually decreased from 3.27 to 2.35 eV with the increase of Cd content x from 0 to 0.44, corresponding to the change of the band gap energy in WZ-phase. With a further increase in the Cd content to x = 0.50, however, the absorption edge energy shows a drastic increase to ~ 3.0 eV. This can be attribute to a phase transition from the low gap WZ phase to a high gap RS phase [1]. However, because the increase of absorption

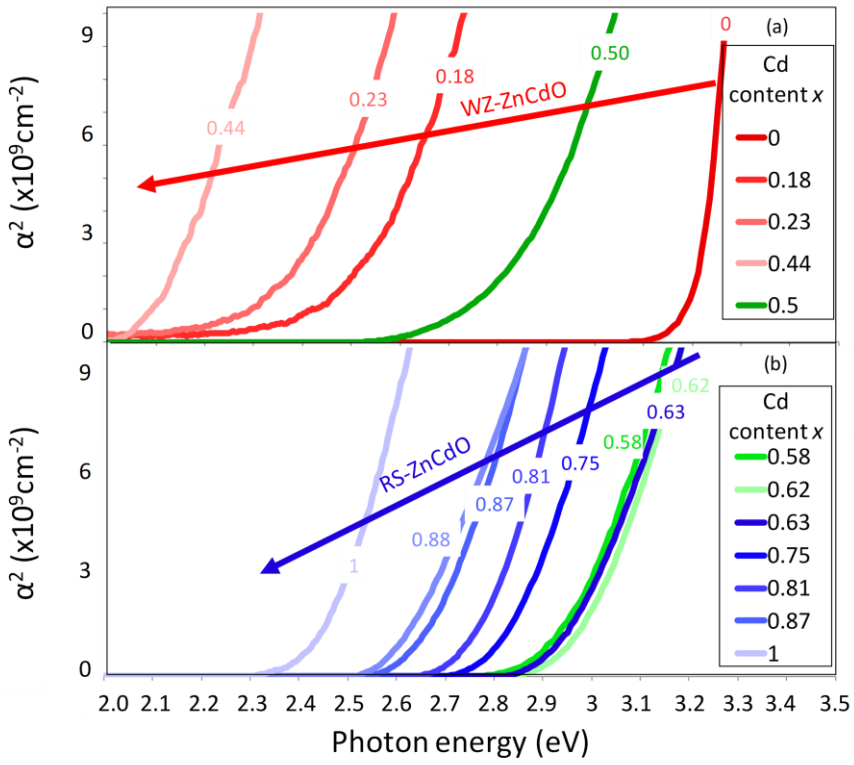

Figure 3.5 Optical absorption spectra of ZnCdO with (a) $x \leq 0.5$ and (b) $x \geq 0.58$.

coefficient near the absorption edge is not very steep as compared to other RS samples, we suppose this sample has a mixed phase. On the other hands, the ZnCdO with $x \geq 0.58$ shows a steep increase of absorption coefficients above the absorption edge energy, and the absorption edge energy gradually decreases again with increasing Cd content. Therefore, this region is considered as a pure RS phase region.

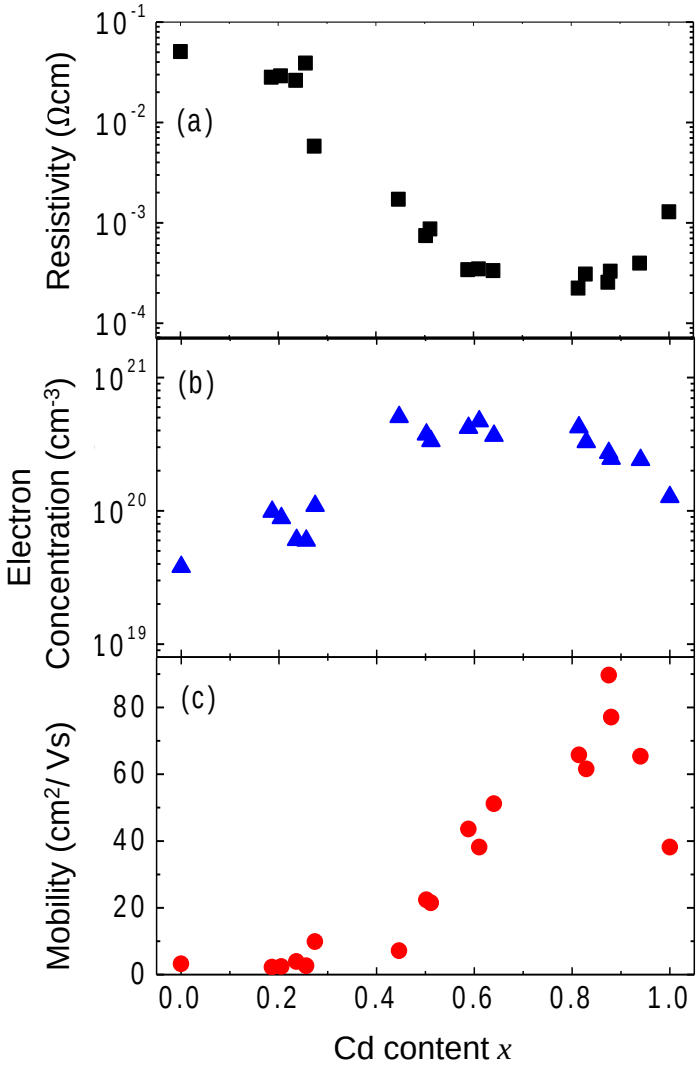

Figure 3.6 Resistivity, electron concentration and mobility of ZnCdO thin films on α-Al_2O_3 (0001) substrate measured by hall effect measurement.

The results of Hall effect measurement are illustrated in Fig. 3.6. All the ZnCdO films showed an *n*-type conductivity. The resistivity decreased gradually with increasing Cd content *x* from 0 to 0.58, then it becomes saturated at very a low resistivity of around 5×10^{-4} Ωcm in the RS phase. The electron concentration is in the range between 4×10^{19} cm^{-3} and 1×10^{20} cm^{-3} in RS phase. The mobility of WZ-ZnCdO was very low and less than 10 cm^2/Vs. in contrast, for RS phase alloys, the mobility increased to ~ 90 cm^2/Vs. Such high mobility is consistent with other report for RS-ZnCdO [1].

The optical band gap of the films was determined by applying the Tauc model [9] or the Davis-Mott model [10] in the high absorbance region:

$$\alpha \mathrm{hv} = \mathrm{D}\left(\mathrm{hv} - E_g\right)^n \qquad (1)$$

where D is a constant and *n* is the power index for direct-allowed transition as *n*=1/2 was found to be more suitable for ZnCdO, giving the best linear approximation of the band-edge [11]. Consequently, *n*=1/2 is employed for fitting of experimental data, and the obtained optical band gaps were presented in Fig. 3.7 as a function of Cd content *x* by black circles with error-bars.

When the Cd content x is zero, an optical band gap energy of 3.27 eV was obtained, which agrees well with the reported band gap energy of WZ-ZnO [1]. The optical band gap energy decreases gradually with increasing the Cd content *x* in WZ region. When the Cd content exceeds around 0.5, the optical band gap energy rapidly increased as mentioned above. In the RS region, the optical band gap energy decreases again with the increases of Cd content.

According to the theoretical calculation [12,13,14,15], it is reported that the WZ-ZnO (WZ-CdO) has a higher direct band gap than RS-ZnO (RS-CdO) because, in WZ structure, the valence

band maxima (VBM) is pushed up due to *p-d* repulsion resulting from the hybridization of O 2*p* state and metal *d* state, reducing the fundamental direct gap. In the RS structure, the respective states do not hybridize and the *p-d* repulsion and the corresponding gap shrinkage vanishes at zone center (Γ) because of its symmetry forbiddance. This is the main reason for the rapid increase of the optical band gap energy by the phase transition from WZ to RS. However, it is also reported that, in RS structure, in other regions of the Brillouin-zone, the bands are subject to the *p-d* repulsion and thereby raised at points away from Γ, leading the material to the indirect gap semiconductor. In our optical absorption spectra for RS-ZnCdO, the indirect absorption was not clearly observed, probably due to a very weak absorption for the indirect transition.

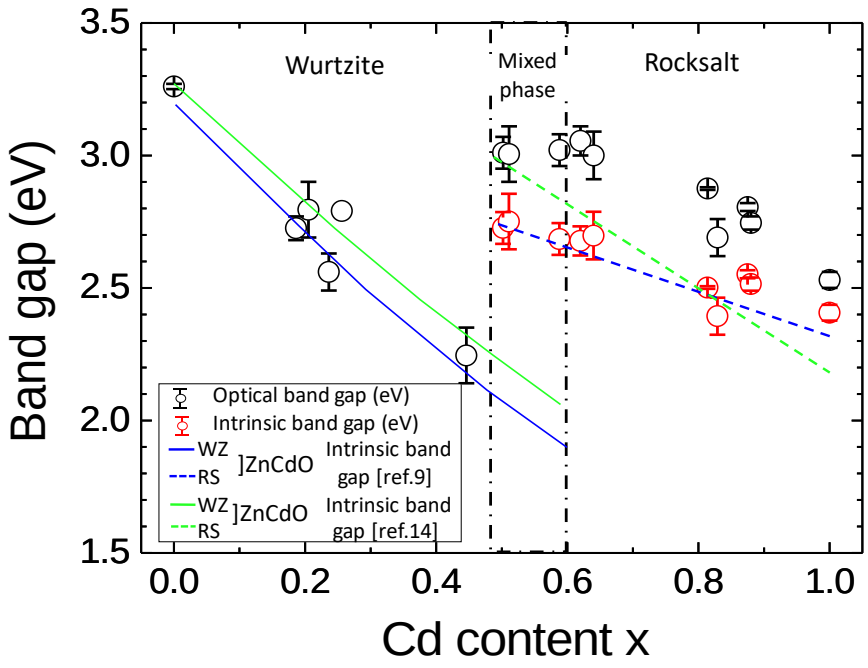

Figure 3.7 Optical and intrinsic band gap energies of ZnCdO thin films on α-Al_2O_3 (0001) substrate under various Cd content. Solid and dashed lines are reported intrinsic band gap of WZ- and RS- ZnCdO from ref.9 (blue) and ref.14 (green), respectively.

It should be noted that the higher optical band gap energies are observed for RS-ZnCdO alloys (~ 3.0 eV for x~0.6) as compared to other reports [1,7,16], which is consistent with the phase transition composition with lower x than other reports. The stability of the RS phase at such low Cd content may be attributed to the non-equilibrium MBE growth at a relatively low temperature of 250 °C. Also, in the mixed phase sample of ZnCdO with x~0.5, the optical band gap is determined by RS-ZnCdO phase with a smaller band gap energy. Therefore, the obtained band gap is close to those for RS-ZnCdO with x~0.6.

The obtained optical band gap energies for the RS phase alloys are larger than the reported intrinsic energies [1,8,16,17,18,19], as shown by blue and green dashed lines in Fig. 3.7. This arises from free carrier effects in these alloys, namely the Burstein-Moss shift, and band renormalization, sine the electron concentration is higher than 10^{20} cm^{-3} for the RS-ZnCdO alloys.

The intrinsic band gaps of ZnCdO were calculated for all thin films by considering free carrier effects using similar procedures as reported in Ref. 12 and Ref.14, and are shown by red circle with error-bars in Fig. 3.7. The intrinsic band gap of ZnCdO thin films on α-Al_2O_3 (0001) substrate by MBE agree well with previous reports [1,20].

Figure 3.8 compares transmittance spectra of RS-ZnCdO and AZO thin films with similar carrier concentration. It can be seen that RS-ZnCdO thin films has higher transmittance around 80 ~ 95% in the wavelength region from 500 nm to 2000 nm as compared to AZO. Especially, the IR transmission of RS-ZnCdO is much higher than AZO. This is because of lower electron effective mass, higher static dielectric constant and higher high frequency permittivity of RS-ZnCdO, which can be expected from those of RS-CdO (m_e^*=0.21m_0 [21], ε = 21.9, ε_∞ = 5.3[22]), than WZ-ZnO

(m_e^*=0.29m_0 [23], ε = 8.75, ε_∞ = 3.75 [24]), leading to the decrease of FCA by a higher mobility and a longer plasma wavelength [15].

Also, RS-ZnCdO in this study shows around 20% higher transmittance overall than the reported transmittance of RS-ZnCdO [25]. However, due to the lower intrinsic gap of ~ 2.5 eV, the transmittance in UV region is limited to < 400 nm as compared with AZO and further improvement is required. For example, for a RS-ZnCdO with x ~ 0.6, the intrinsic gap is ~ 2.7 eV and with extrinsic doping to a high electron concentration of 10^{21} cm^{-3}, its absorption edge can be increased to > 3.5 eV (or < 350 nm). Also, the RS phase may be extended to smaller Cd region by growing on a cubic substrate, widely used for MJSCs, instead of hexagonal α-Al_2O_3 (0001)

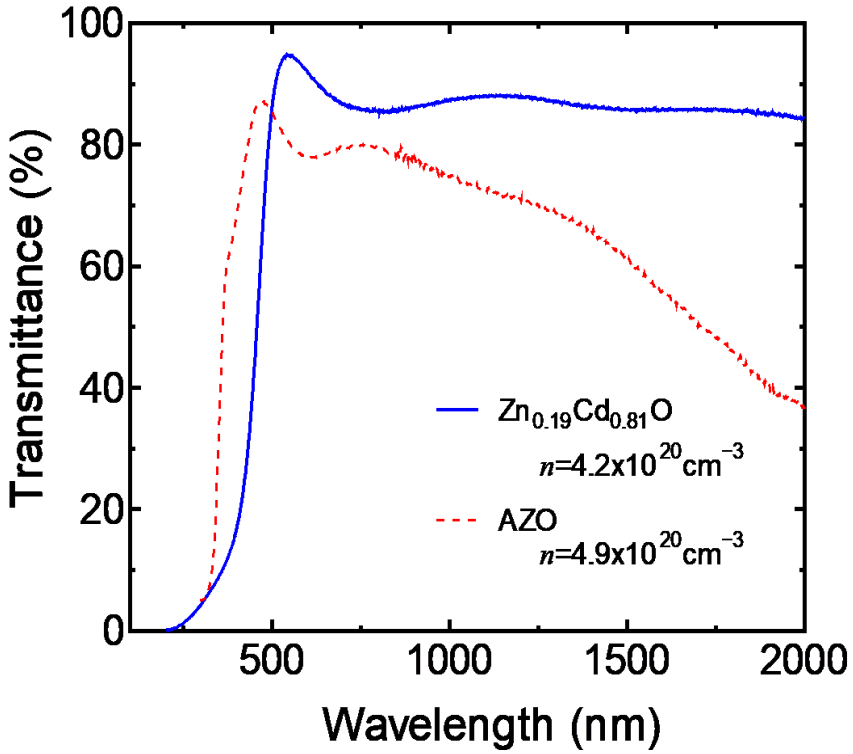

Figure 3.8 Typical transmittance spectra of RS-ZnCdO and AZO thin films with similar electron concentration.

substrates. The desirable properties of larger band gap energy, low resistivity, high mobility, and high transmittance in a wide spectral range make the RS-ZnCdO thin films promising candidate as TCOs for devices requiring a high conductivity and a wide transparency window, such as MJSCs.

3.4 Conclusion

ZnCdO thin films were grown on α-Al_2O_3 (0001) substrate by molecular beam epitaxy with various Cd content. The phase transition from wurtzite to rocksalt is found to take a place at the Cd content x ~ 0.5 to 0.6. Within the composition region of x ~ 0.5 to 0.6, both RS and WZ crystals co-exist. Transmittance above 80 ~ 95 % in the visible range is observed for both the WZ and RS alloys. Optical gap of the WZ alloys decreases from 3.27 eV for ZnO to ~ 2.35 eV (x ~ 0.44). At the phase transition to RS at x ~ 0.55, the optical gap increases drastically to > 3.0 eV RS-alloys with a large optical gap of 3.0 eV (an intrinsic gap of ~ 2.7 eV) is achieved for x ~ 0.6. RS-ZnCdO thin films exhibit a low resistivity of 5×10^{-4} Ωcm with a maximum mobility of ~ 90 cm^2/Vs and a high carrier concentration 4×10^{20} cm^{-3}. These properties make RS-ZnCdO potentially useful TCO materials for full spectral solar cells.

Reference

[1] D. M. Detert, K. B. Tom, C. Battaglia, J. D. Denlinger, S. H. N. Lim, A. Javey, A. Anders, O. D. Dubon, K. M. Yu, W. Walukiewicz, "Crystal structure and properties of $Cd_xZn_{1-x}O$ alloys across the full composition range", Appl. Phys. Lett, **102**, 2013, 232103, https://doi.org/10.1063/1.4809950

[2] Y. Chen, S. Zhang, W. Gao, F. Ke, J. Yan, B. Saha, C. Ko, J. Suh, B. Chen, J. W. Ager III, W. Walukiewicz, R. Jeanloz, and J. Wu, "Pressure-induced structural transition of $Cd_xZn_{1-x}O$ alloys", Appl. Phys. Lett. **108**, 2016, 152105, https://doi.org/10.1063/1.4947022

[3] D. M. Detert. K. B. Tom, C. Battaglia, J. D. Denlinger, S. H. N. Lim, A. Javey, A. Anders, O. D. Dubon, K. M. Yu, and W. Walukiewicz, "Fermi level stabilization and band edge energies in $Cd_xZn_{1-x}O$ alloys", J. Appl. Phys. **115**, 2014, 233708, https://doi.org/10.1063/1.4884683

[4] M. D. C. M. Tomas, A. H. Barbera. S. Agouram and V. M. Sanjose, "Induced crystallographic changes in $Cd_{1-x}Zn_xO$ films grown on r-sapphire by AP-MOCVD: the effects of the Zn content when $x \leq 0.5$", CrystEngComm, **22**, 2020, 74-78, https://doi.org/10.1039/C9CE01483G

[5] J. W. Min, S. Y. Bae, W. M. Kang, K. W. Park, E. K. Kang, B. J. Kim, D. S. Lee, Y. T. Lee, "Evolutionary Growth of Microscale Single Crystalline GaN on Amorphous Layer by Combination of MBE and MOCVD", CrystEngComm, **30**, 2015, 5849-5859, https://doi.org/10.1039/C5CE00543D

[6] A.G. S. Kumar, T. S. Sarmash, L. Obulapathi, D. J. Rani, T. S. Rao, K. Asokan, "Effect of substrate temperature on structural and optical properties of reactive dc magnetron sputtered CdZnO thin films", Materials Today: Proceedings. **3**, 2016, 1604–1608, https://doi.org/10.1016/j.matpr.2016.04.049

[7] T. Liu, D. Wang, F. Guo, S. Jiao, J. Wang, Y. Liu, C. Luan, W. Cao, L. Zhao, "Effect of annealing temperature on the optical property of high Cd content CdZnO films", Super lattices and Microstructures, **97**, 2016, 569-574, DOI: 10.1016/j.spmi.2016.07.010

[8] C. Y. Ho, C. P. Liu, Y. C. Chen, Z. Q. Huang, F. C. Chuang, K. M. Yu, "Effects of oxygen stoichiometry on the phase stability of sputter-deposited $Cd_xZn_{1-x}O$ alloys", Phys. Rev. Materials, **3**, 2019, 074605, https://doi.org/10.1103/PhysRevMaterials.3.074605

[9] J. Tauc, "Amorphous and Liquid Semiconductors", Plenum, London (1974).

[10] E.A Davis, N.F. Mott, "Conduction in non-crystalline systems V. Conductivity, optical absorption and photoconductivity in amorphous semiconductors", Philos. Mag., **22**, 1970, 903, https://doi.org/10.1080/14786437008221061

[11] V. Venkatachalapathy, A. Galeckas, R. Sellappan, D. Chakarov, A. Yu. Kuznetsova, "Tuning light absorption by band gap engineering in ZnCdO as a function of MOVPE-synthesis conditions and annealing", J. Cryst. Growth, **315**, 2011, 301-304, DOI: 10.1016/j.jcrysgro.2010.09.056

[12] A. Schleife, F. Fuchs, J. Furthmüller, and F. Bechstedt, "First-principles study of ground- and excited-state properties of MgO, ZnO, and CdO polymorphs", Phys. Rev. **B73**, 2006 245212, https://doi.org/10.1103/PhysRevB.73.245212

[13] S.-H. Wei and Alex Zunge, "Role of metal d states in II-VI semiconductors", Phys. Rev. **B37**, 1988, 8958, DOI: 10.1103/physrevb.37.8958

[14] Y. Z. Zhu, G. D. Chen, Honggang Ye, Aron Walsh, C. Y. Moon, and Su-Huai Wei, "Electronic structure and phase stability of MgO, ZnO, CdO, and related ternary alloys", Phys. Rev. **B77**, 2008, 245209, https://doi.org/10.1103/PhysRevB.77.245209

[15] P. D. C. King, T. D. Veal, A. Schleife, J. Zúñiga-Pérez, B. Martel, P. H. Jefferson, F. Fuchs, V. Muñoz-Sanjosé, F. Bechstedt, and C. F. McConville, "Valence-band electronic structure of CdO, ZnO, and MgO from x-ray photoemission spectroscopy and quasi-particle-corrected density-functional theory calculations", Phys. Rev. **B79**, 2009, 205205, https://doi.org/10.1103/PhysRevB.79.205205

[16] D. S. Ginley, H. Hosono, D. C. Paine, "Handbook of Transparent Conductors", Springer, New York, 2011.

[17] D. T. Speaks, M. A. Mayer, K. M. Yu, S. S. Mao, E. E. Haller, W. Walukiewicz, "Fermi level stabilization energy in cadmium oxide", J. Appl. Phys. **107**, 2010, 113706, https://doi.org/10.1063/1.3428444

[18] A. Segura, J. F. Sanchez-Royo, B. Garcia-Domene, G. Almonacid, "Current underestimation of the optical gap and Burstein-Moss shift in CdO thin films: A consequence of extended misuse of α^2-versus-hν plots", Appl. Phys. Lett, **99**. 2011, 151907, https://doi.org/10.1063/1.3651338

[19] C. P. Liu, Y. Foo, M. Kamruzzaman, C. Y. Ho, J. A. Zapien, W. Zhu, Y. J. Li, W. Walukiewicz. K. M. Yu, "Effects of Free Carriers on the Optical Properties of Doped CdO for Full-Spectrum Photovoltaics", Phys. Rev. Appl. **6**, 2016, 064018, https://doi.org/10.1103/PhysRevApplied.6.064018

[20] S. Patil, S. Raut, R. Gore, B. Sankapal, “One-dimensional cadmium hydroxide nanowires towards electrochemical supercapacitor”, New J. Chem., **39**, 2015, 9124, https://doi.org/10.1039/C5NJ02022K

[21] S. K. V. Farahani, V. Munoz-Sanjose, J. Zuniga-Perez, C. F. McConville, and T. D. Veal, “Temperature dependence of the direct bandgap and transport properties of CdO”, Appl. Phys. Lett. **102**, 2013, 022102, https://doi.org/10.1063/1.4775691

[22] H. Finkenrath, in Physics of II-VI and I-VII Compounds, “Semi-Magnetic Semiconductors, Landolt-Bornstein: Numerical Data and Functional Relationships in Science and Technology”, Group III: Crystal and Solid State Physics, Springer, Berlin, 1982, Vol. 17B.

[23] W. S. Baer, “Faraday Rotation in ZnO: Determination of the Electron Effective Mass”, Phys. Rev. **154**, 1967, 785, https://doi.org/10.1103/PhysRev.154.785

[24] K. Ellmer, A. Klein, B. Rech, “Transparent Conductive Zinc Oxide”, Springer, Berlin 2008, https://link.springer.com/book/10.1007/978-3-540-73612-7

[25] R.K. Gupta, M. Cavas, F. Yakuphanoglu, “Structural and optical properties of nanostructure CdZnO films”, Molecular and Biomolecular Spectroscopy, **9**, 2012, 107-113, DOI: 10.1016/j.saa.2012.04.012

Chapter 4

Structural, Optical, and Electrical properties of WZ- and RS-ZnCdO thin films on MgO (100) substrate by molecular beam epitaxy

4.1 Introduction

In the previous **Chapter 3**, the growth of ZnCdO thin films are established on α-Al_2O_3 (0001) substrate by molecular beam epitaxy with various Cd content, and large optical band gap energy of 3.0 eV (an intrinsic band gap energy of ~ 2.7 eV) was obtained in poly-crystalline RS-ZnCdO thin film. Although this optical band gap is the highest ever reported for RS-ZnCdO [1,2,3,4], it is still lower than that for other TCOs and further improvement is necessary. Therefore, several studies have been established to expend the band gap of ZnCdO.

In this study, we have changed substrate from sapphire to Rockslat (RS) -MgO substrate. Since the band gap of RS-ZnCdO increases with Zn composition in the alloy, it is desirable to grow ZnCdO on a RS substrate to achieve a single-crystalline RS-ZnCdO alloy with high Zn content. As the substrate, MgO with a RS structure (a = 4.21 Å) is a suitable material. The lattice mismatch between RS-MgO and RS-CdO is 11.6%, and it decreases with increasing Zn composition in RS-ZnCdO. In this study, the growth of single-crystalline RS-ZnCdO on RS-MgO substrate is investigated.

In this chapter, ZnCdO thin films grown on MgO (100) substrate to promote the crystallinity and extend the RS phase composition by growing on a RS-MgO substrate by MBE. The structural, optical, and electrical properties with phase transition of WZ- and RS-ZnCdO thin films were clarified concretely through a variety of characterization methods.

4.2 Experimental

A conventional MBE system with a radio frequency (RF) radical cell for oxygen was used to grow ZnCdO thin films on MgO (100) substrates with the thickness of 0.5 mm. Before introducing MgO (100) substrates inside to the MBE growth chamber, the substrates were cleaned in organic solvents by ultrasonic cleaner. Cd (6N) and Zn (7N) were used as source materials. The background pressure was controlled less than 6×10^{-8} Pa in the growth chamber. The oxygen was supplied constantly by the RF radical cell as flow rate of 0.3 sccm with 300 W of the RF power. The Cd flux ratio ($f_{Cd} = \frac{[Cd\ flux]}{[Cd\ flux]+[Zn\ flux]}$) was controlled in the range from 0 to 1 to grow different Cd composition of ZnCdO thin films. During the growth, the substrate temperature was maintained at 250°C, which is the optimized temperature for the growth of ZnCdO by MBE [5].

To characterize the surface crystallinity, a reflection high-energy electron diffraction (RHEED) was monitored during the MBE growth. A surface step profiler was used to measure the thickness of ZnCdO thin films after the growth. The energy dispersive X-ray spectroscopy (EDX) was conducted to analyze the Cd composition. The crystal structures of ZnCdO thin films were analyzed using a conventional θ-2θ X-ray diffraction (XRD) with a Cu Kα radiation. Double-beam spectrophotometer was used for reflectance and transmittance measurements in the wavelength

range between from 200 to 2000 nm, and the baseline correction using bare MgO substrates was performed to eliminate the effect of absorption by the substrate. Optical absorption coefficient (α) was obtained using the reflectance, transmittance, and thickness, and the band gap energy of films was deduced by a square plot of α. For the characterization of electrical properties, a hall effect measurement using the Van der Pauw configuration was conducted with In as ohmic contact at room temperature.

4.3 Results and discussion

All ZnCdO thin films on MgO substrates showed a thickness of around 60 nm. The Cd composition *x* in the films by EDX analyses are presented at Fig. 4.1 under the various Cd flux.

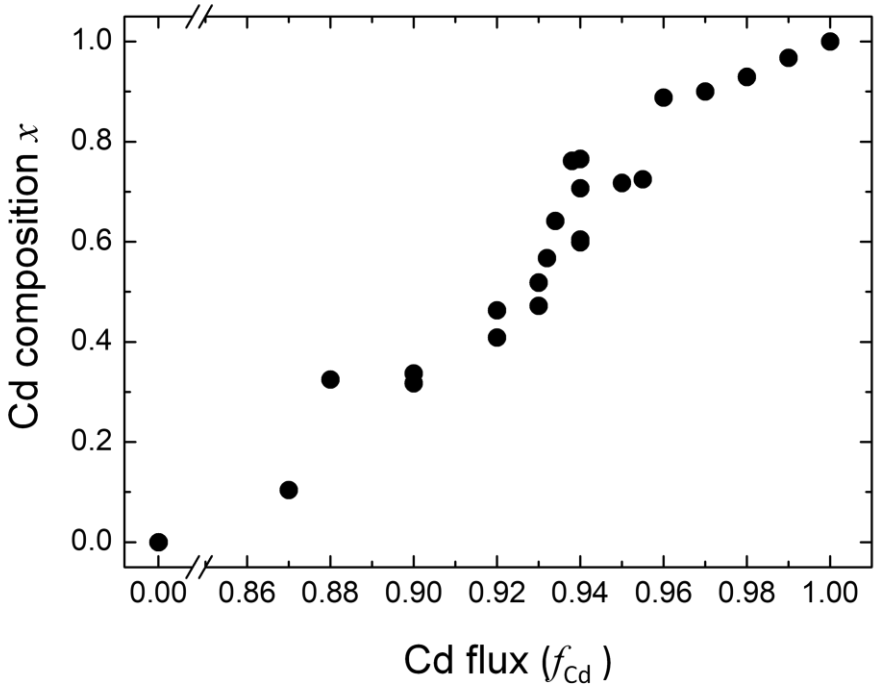

Figure 4.1 Cd composition *x* in ZnCdO thin films on MgO (100) substrates determined by EDX measurements.

As the f_{Cd} decreases from 1 to 0.87, the Cd composition x in films decreases steadily from 1 to 0.1 and 0 at f_{Cd} = 0. This tendency is similar to our previous results obtained for MBE growth of ZnCdO on sapphire substrates [5]. Therefore, the various composition of ZnCdO films can be grown on MgO (100) substrates by adjusting the f_{Cd}.

Figures 4.2 (a) ~ (f) show the RHEED patterns of ZnCdO films under the different Cd composition x from 0.1 to 0.72 on MgO (100) substrates. ZnCdO films with $x \geq 0.59$ showed a spot pattern corresponding to RS structure, indicating the epitaxial growth of single-crystalline RS-ZnCdO. For the film with x = 0.56, the RHEED pattern changed to a weak ring pattern with very weak spot, and at x = 0.51, the spotty patter became predominant although the pattern was still halo-like. Further decrease of Cd composition x led to a rather clear spotty pattern. These RHEED pattern in Figs. 4.2 (a) and (b) is similar to that reported for *c*-axis oriented WZ-ZnO on

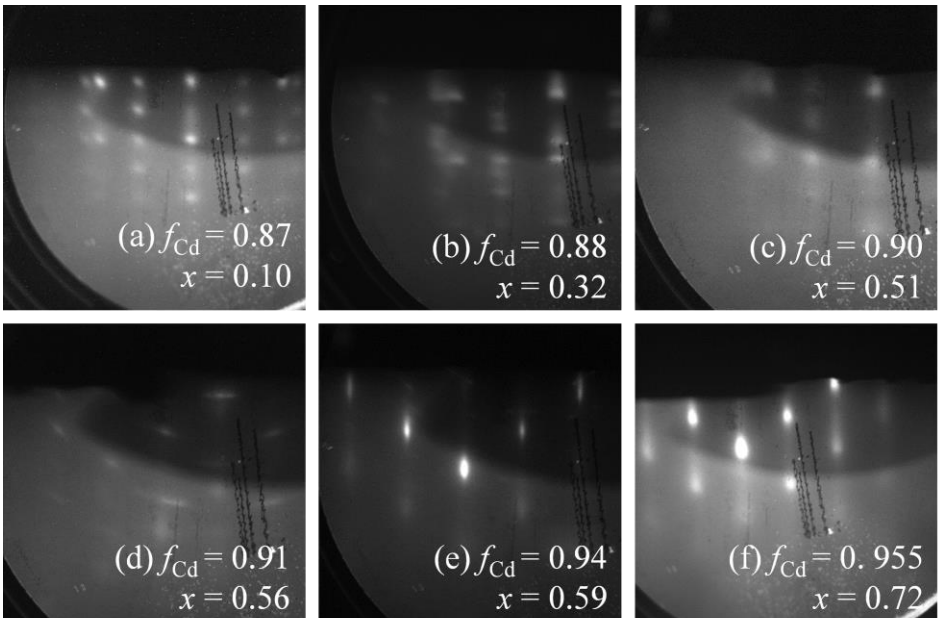

Figure 4.2 RHEED patters after growth of ZnCdO thin films under the various f_{Cd} and Cd composition. The electron beam was reflected along the [011] azimuth.

MgO (100) with two kinds of domains [6], suggesting the growth of *c*-axis oriented WZ-ZnCdO in these Cd composition regions.

Typical XRD profiles of ZnCdO films on MgO (100) substrates with various Cd compositions are presented in Fig. 4.3 (a). In the CdO film with $x = 1$, only the peak at 38.45° corresponding to RS-CdO (200) was observed. The lattice parameter *a* obtained for this sample was 4.69 Å, consistent with the reported value of 4.696 Å [7] for RS-CdO. With decreasing Cd composition down to $x = 0.59$, diffraction peak shifted to higher angle side up to 39.11° suggesting

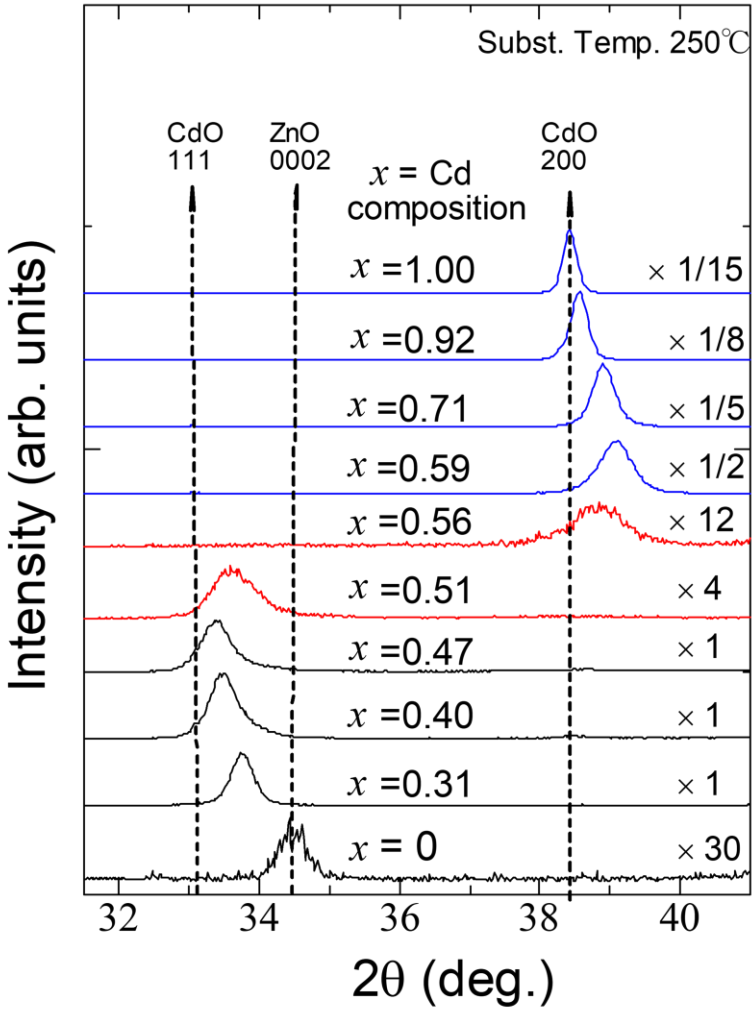

Figure 4.3 (a) XRD profiles of ZnCdO films on MgO (100) substrates.

a decrease of lattice parameter duo to the replacement of Cd by Zn. The change of the lattice parameter along with Vegard's law under different Cd composition is plotted in Fig. 4.3 (b) as blue triangles. Along with the decrease of Cd composition, the lattice parameter decreases linearly. At Cd composition x = 0.56, the diffraction peak was not following the trend but appeared at slightly lower angle of 38.84° with very weak intensity. This change is consistent with the RHEED observation, and may indicate a phase transition from RS phase to WZ phase, and at this composition both phases may co-exist. When the Cd composition decreases further to x = 0.51, the peak corresponding to the RS (200) diffraction disappeared and a completely different peak was observed at 33.6° with also weak intensity.

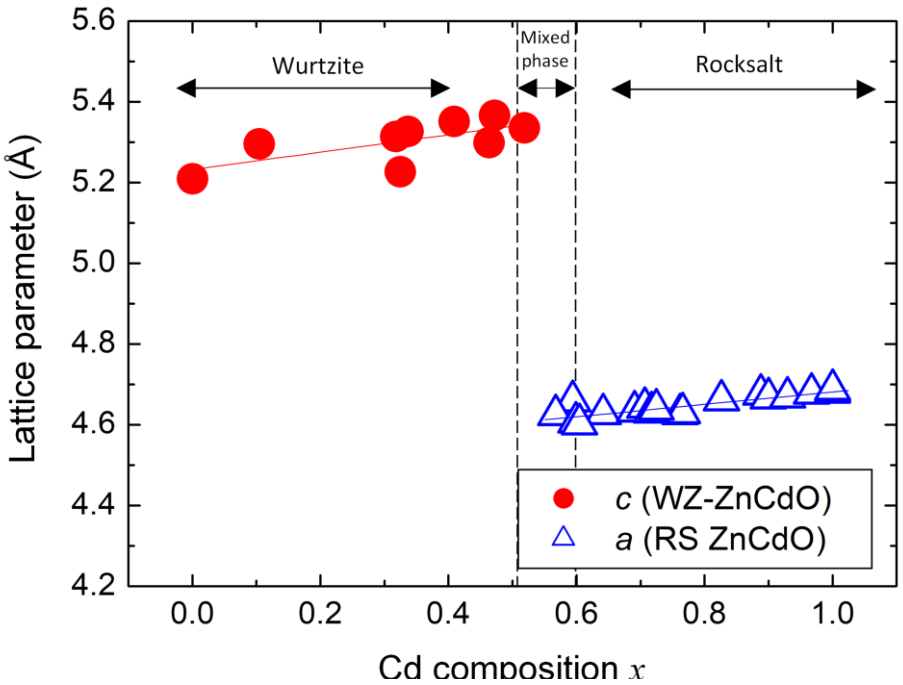

Figure 4.3 (b) Calculated lattice parameters by XRD profiles of ZnCdO films on MgO (100) substrates.

In the ZnO film with x = 0, only the WZ-ZnO (0002) diffraction peak was observed at 34.4°. This result is consistent with the previous study of ZnO grown on sapphire [5], although the diffraction intensity is much lower than the film on sapphire substrate presumably due to the growth on different crystal system. By the increase of Cd composition up to x = 0.47, the diffraction peak moved to lower angle side down to 33.3°. The change of the lattice parameter is presented in Fig. 4.3(b) as red circles. The lattice parameter changes almost linearly in this region, indicating the inclusion of more Cd with a larger ionic radius in the Zn sublattice of WZ-ZnCdO [8,9]. The observed growth of *c*-axis oriented WZ-ZnCdO is consistent with the RHEED results. At Cd composition x = 0.51, the XRD peak appeared at slightly higher angle of 33.6° with weaker intensity. This change is similar to the film with x = 0.56 in RS-phase side, and may indicate the phase transition at this composition.

Figure 4.4 shows the resistivity, electron concentration and electron mobility of ZnCdO films on MgO (100) substrates. The results obtained on sapphire substrates described in **Chapter 3** [5] are also shown for comparison. An *n*-type conductivity was confirmed to all the ZnCdO films. ZnCdO films with $0 \leq x \leq 0.1$ showed high resistivity over 1.3×10^2 Ωcm. This is due to the low electron concentration ($< 10^{17}$ cm^{-3}) of these films. With increasing Cd composition, the resistivity decreases gradually in the WZ phase, and in the RS phase ($x \geq 0.59$), it becomes settled at a very low resistivity of around 2.5×10^{-4} Ωcm. The RS-ZnCdO films showed a high electron concentration from 1.3×10^{20} to 1.5×10^{21} cm^{-3}. Although the mobilities of WZ-ZnCdO with $0 \leq x \leq 0.51$ was very low and less than 17.7 cm^2/Vs, those for RS phase alloys ($0.59 \leq x \leq 1.0$) increased to ~ 51.7 cm^2/Vs. Such properties of high electron concentration and high mobility are

constant with the previous report on sapphire substrates [5] and also other report for RS-ZnCdO on glass substrates [1].

Figure 4.5 shows the typical transmittance of ZnCdO films on RS phase with x = 0.60 and 0.76 and WZ phase with x = 0.46. High transmittance around 80% in visible region (500 ~ 700nm)

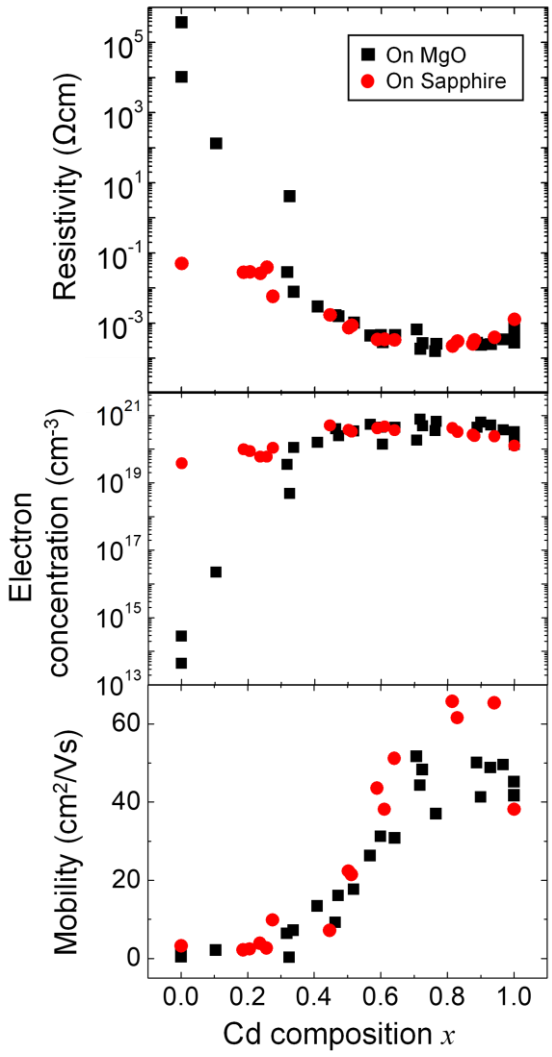

Figure 4.4 Resistivity, electron concentration, and electron mobility of ZnCdO films. The results on MgO (100) substrates are presented as black squares whereas those on sapphire substrates are shown as red circles for comparison.

and 85% in infrared region (700 ~ 2000 nm) were observed on both RS-ZnCdO thin films, whereas WZ-ZnCdO thin film show lower transmittance in whole wavelength range.

In Figs. 4.6 (a) and (b), the optical absorption spectra of ZnCdO films for $x \leq 0.51$ and $x \geq 0.51$ are shown, respectively. In Fig. 4.6 (a), the energy of the absorption edge progressively decreases from 3.3 eV of ZnO to 2.16 eV with the increase f_{Cd} composition x from 0 to 0.51, indicating the change of the band gap energy in WZ phase. Especially, the film with x = 0.51 showed a clear optical absorption spectrum as WZ-ZnCdO without any sub-absorption although it was suspected to be a mixed phase from RHEED and XRD results. So, most part of this film is considered to consist of WZ-ZnCdO. However, drastic increases of the absorption edge energy from 2.16 eV to 3.08 eV are observed when the Cd composition increases from x = 0.51 to x = 0.59 due to a phase transition from the low gap WZ phase to a high gap RS phase [1], as shown in Fig. 4.6 (b). The film with Cd composition x = 0.56 is considered to have a mixed phase because

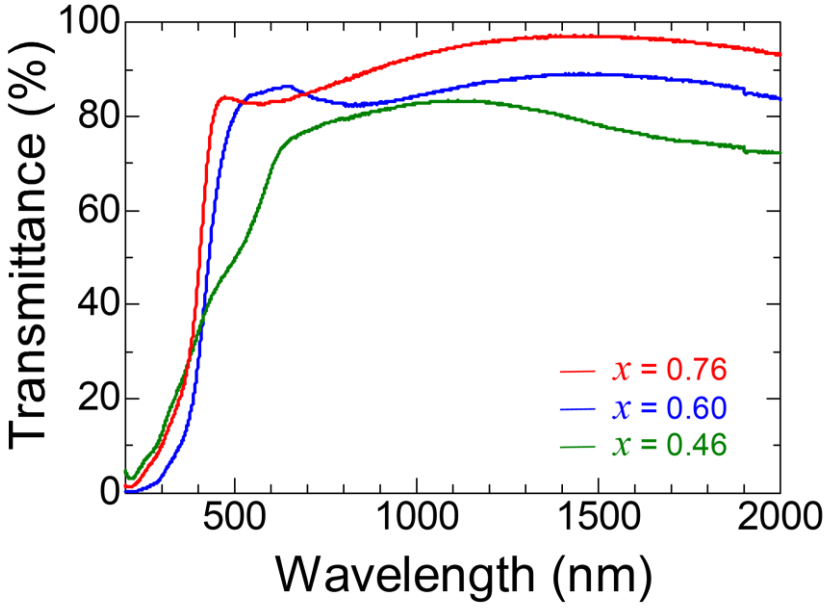

Figure 4.5 Transmittance of RS-ZnCdO at x = 0.76, 0.60 and WZ-ZnCdO at x = 0.46.

the absorption coefficient does not increase steeply near the absorption edge compared with other WZ or RS. Figure 4.6(b), when the Cd composition *x* increase more than 0.59, the gradual decrease of absorption edge energy are observed again. Therefore, the film with $x \geq 0.59$ is considered to have a pure RS phase.

Optical band gap energy was determined by the square plot of absorption coefficient (α) using the Tauc model [26] as:

$$\alpha h\nu = D\left(h\nu - E_g\right)^n \quad (1)$$

where, E_g is the optical band gap energy, D is the photon energy independent constant, $h\nu$ is the photon energy, and n depends on the nature of the transition ($n = \frac{1}{2}$ for the direct allowed transition, $n = \frac{2}{3}$ for the direct forbidden transition, and $n = 2$ for the indirect allowed transition). For ZnCdO, it was reported that n = 1/2 is more suitable to achieve the best linear approximation of the band-edge [11]. Thus, n =1/2 is used to fit experimental data. The optical band gap energy obtained for films with high electron concentration (>

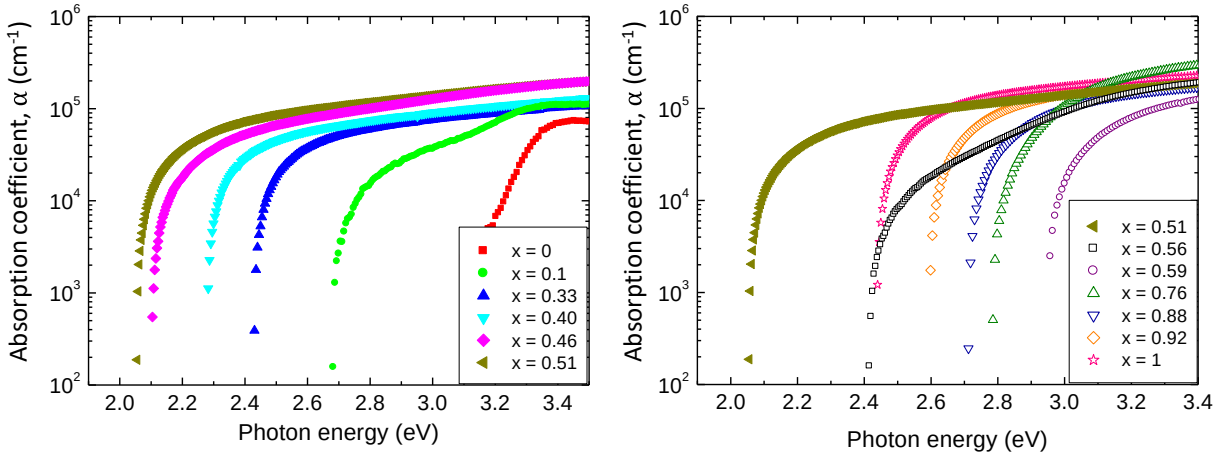

Figure 4.6 Calculated optical absorption spectra of ZnCdO films with (a) $x \leq 0.51$ and (b) $x \geq 0.51$.

10^{19} cm^{-3}) is expected to be higher than the intrinsic band gap energy because of FCA effects including Burstein-Moss shift and band renormalization. The intrinsic band gap energies were also estimated in consideration of FCA effects using the same processes reported in Refs.1 and 12.

Figure 4.7 shows the intrinsic (red triangles) and optical (black circles) band gap energies of ZnCdO films on MgO (100) substrates under different Cd composition. For comparison, the reported intrinsic band gap energies of WZ- [13] and RS-ZnCdO [1] films are also plotted by solid and dashed lines, respectively.

At the Cd composition $x = 0$, an optical band gap energy was obtained as 3.25 eV, in consistent with the band gap energy reported for WZ-ZnO [1,9]. With increasing the Cd composition from 0 to 0.51, the optical band gap energy decreases gradually in WZ region. When the Cd composition exceeds 0.51, the optical band gap energy rapidly increases and the large optical band gap energy of 3.08 eV was obtained at $x = 0.59$ where the intrinsic band gap energy was 2.72eV. Compared to other reports [1,8,13], this is the highest optical band gap energy reported for RS-ZnCdO films. At the Cd composition $x \geq 0.61$, the optical band gap energy becomes smaller again with increasing Cd composition. As shown by red triangles in Fig. 4.7, the intrinsic band gap energies of RS-ZnCdO are almost similar to the intrinsic band gap energies reported so far [1,13].

According to theoretical calculations [9,14,15,16], the direct band gap of RS-ZnO (RS-CdO) is higher than that of WZ-ZnO (WZ-ZnO). The valance band maxima (VBM) in the WZ structure is pushed up and decreases the fundamental direct gap because of *p-d* repulsion arising from the hybridization of metal d and O *2p* states. On the other hands, in the RS structure, due to its symmetry forbiddance, the respective states do not make hybridization and the *p-d* repulsion and the shrinkage of the corresponding band gap disappears at zone center (Γ). This is the main cause for the rapid expansion of the optical band gap due to the phase transition from WZ to RS. Also, the RS structure is reported to be an indirect gap semiconductor because, in other Brillouin-zone regions, the *p-d* repulsion occurs and the bands are raised at points away from Γ. In the optical

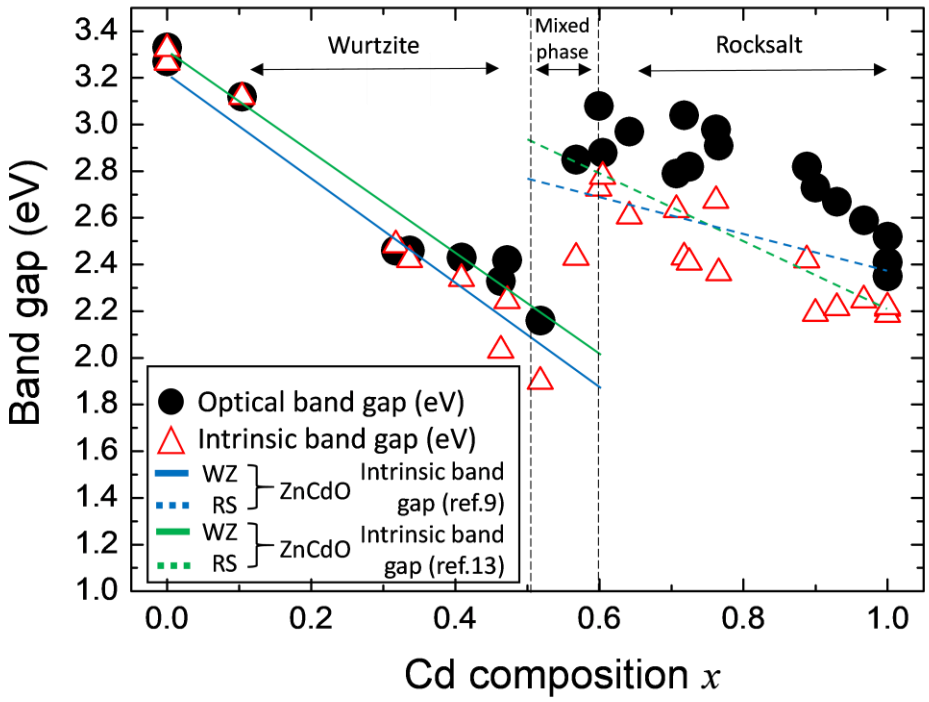

Figure 4.7 Optical and intrinsic band gap energies of ZnCdO thin films on MgO (100) substrates with different Cd composition. The intrinsic band gaps of WZ- and RS-ZnCdO reported in ref. 9 (blue) and ref. 13 (green) are shown by solid and dashed lines, respectively.

absorption spectra for RS-ZnCdO, presumably owing to very weak absorption by the indirect transition, it could not be observed the clear indirect absorption.

By using RS-MgO (100) substrate, the RS-ZnCdO epitaxial films were obtained in Cd composition $0.59 \leq x \leq 1.0$, which is similar composition range reported before on sapphire substrates using MBE [5]. Therefore, it is considered that the phase stability is not influenced significantly by the substrate. According to the DFT calculation [16], RS alloys are reported to be more stable in an O-poor growth environment, and this will limit the lowest Cd composition for the growth of RS-ZnCdO by MBE. Therefore, it may be effective to change the flow rate of oxygen in order to further clarify the phase stability of ZnCdO by MBE growth. It is worth noting that the higher optical band gap energy of 3.08 eV was obtained at $x = 0.59$ on MgO substrate as compared to 3.0 eV obtained on sapphire substrate. This is due to the enhanced Burstein-Moss shift arising from slightly higher carrier concentration of the sample on MgO substrate. Therefore, the further expansion of the optical band gap energy is expected by doping the extrinsic impurity. Such work is strongly desired in the future because the band gap energy is still lower than other TCO materials like AZO. In the **Chapter 5,** Al have been doped to ZnCdO thin films to expand optical band gap energy. The detail experimental method and results of Al-doped ZnCdO thin films are explained in **Chapter 5**.

4.4 Conclusion

ZnCdO thin films with various Cd compositions were grown on MgO (100) substrates by MBE. It was found that the phase transition from WZ to RS occurs at the Cd composition x

between 0.51 and 0.59. In the visible range, high transmittance above 85% was observed for RS-ZnCdO films ($0.59 \leq x \leq 1.0$). In the WZ-phase region, the optical band gap energy decreased from 3.25 eV for ZnO to ~ 2.16 eV for WZ-ZnCdO with $x \sim 0.51$. After the partial phase transition from WZ to RS at $x > 0.51$, the optical band gap energy increased intensely and the largest optical band gap energy of 3.08 eV was obtained for $x = 0.59$ with an intrinsic band gap energy of 2.72 eV. RS-ZnCdO films showed a low resistivity around 2.5×10^{-4} Ωcm with a maximum mobility of ~ 51.7 cm^2/Vs and a high carrier concentration around 5×10^{20} cm^{-3}. These characteristics of RS-ZnCdO are attractive as TCO materials in future full spectrum solar cells.

Reference

[1] D. M. Detert, K. B. Tom, C. Battaglia, J. D. Denlinger, S. H. N. Lim, A. Javey, A. Anders, O. D. Dubon, K. M. Yu, W. Walukiewicz, "Crystal structure and properties of $Cd_xZn_{1-x}O$ alloys across the full composition range", Appl. Phys. Lett. **102**, 2013, 232103, https://doi.org/10.1063/1.4809950

[2] Y. Chen, S. Zhang, W. Gao, F. Ke, J. Yan, B. Saha, C. Ko, J. Suh, B. Chen, J. W. Ager III, W. Walukiewicz, R. Jeanloz, and J. Wu, "Pressure-induced structural transition of $Cd_xZn_{1-x}O$ alloys", Appl. Phys. Lett. **108**, 2016, 152105, https://doi.org/10.1063/1.4947022

[3] D. M. Detert. K. B. Tom, C. Battaglia, J. D. Denlinger, S. H. N. Lim, A. Javey, A. Anders, O. D. Dubon, K. M. Yu, and W. Walukiewicz, "Fermi level stabilization and band edge energies in $Cd_xZn_{1-x}O$ alloys", J. Appl. Phys. **115**, 2014, 233708, https://doi.org/10.1063/1.4884683

[4] M. D. C. M. Tomas, A. H. Barbera. S. Agouram and V. M. Sanjose, "Induced crystallographic changes in $Cd_{1-x}Zn_xO$ films grown on r-sapphire by AP-MOCVD: the effects of the Zn content when $x \leq 0.5$", CrystEngComm. **22**, 2020, 74, https://doi.org/10.1039/C9CE01483G

[5] H. C. Jang, K. Saito, Q. Guo, K. M. Yu, W. Walukiewicz, T. Tanaka, "Realization of rocksalt $Zn_{1-x}Cd_xO$ thin films with optical band gap above 3.0 eV by molecular beam epitaxy", CrystEngComm, **22**, 2020, 2781, https://doi.org/10.1039/C9CE02018G

[6] H. Zhou, H. Q. Wang, L. Wu, L. Zhang, K. Kisslinger, Y. Zhu, X. Chen, H. Zhan, and J. Kang, "Wurtzite ZnO (001) films grown on cubic MgO (001) with bulk-like opto-electronic properties", Appl. Phys. Lett., **99**, 2011, 141917, https://doi.org/10.1063/1.3647846

[7] J. Zhang, “Room-temperature compressibilities of MnO and CdO: further examination of the role of cation type in bulk modulus systematics”, Phys. Chem. Miner, **26**, 1999, 644, https://doi.org/10.1007/s002690050229

[8] T. Liua, D. Wang, F. Guo, S. Jiao, J. Wang, Y. Liu, C. Luan, W. Cao, L. Zhao, “Effect of annealing temperature on the optical property of high Cd content CdZnO films, Super lattices and Microstructures”, Super lattices and Microstructures, **97**, 2016, 569-574, https://doi.org/10.1016/j.spmi.2016.07.010

[9] A. Schleife, F. Fuchs, J. Furthmüller, and F. Bechstedt, “First-principles study of ground- and excited-state properties of MgO, ZnO, and CdO polymorphs”, Phys. Rev. **B**73, 2006, 245212 https://doi.org/10.1103/PhysRevB.73.245212

[10] J. Tauc, Amorphous and Liquid Semiconductors, Springer, London & New York, 1974.

[11] V. Venkatachalapathy, A. Galeckas, R. Sellappan, D. Chakarov, A. Yu. Kuznetsova, “Tuning light absorption by band gap engineering in ZnCdO as a function of MOVPE-synthesis conditions and annealing”, J. Cryst. Growth, **315**, 2011, 301-304, https://doi.org/10.1016/j.jcrysgro.2010.09.056

[12] K. M. Yu, M. A. Mayer. D. T. Speaks, H. He, R. Zhao, L. Hsu, S. S. Mao, E. E. Haller, W. Walukiewicz, “Ideal transparent conductors for full spectrum photovoltaics”, J. Appl. Phys, **111**, 2012. 123505, https://doi.org/10.1063/1.4729563

[13] D. S. Ginley, H. Hosono, D. C. Paine, “Handbook of Transparent Conductors”, Springer, New York, 2011.

[14] S.H. Wei and A. Zunge, “Role of metal d states in II-VI semiconductors”, Phys. Rev. **B37**, 1988, 8958, https://doi.org/10.1103/PhysRevB.37.8958

[15] Y. Z. Zhu, G. D. Chen, H. G. Ye, A. Walsh, C. Y. Moon, and S. H. Wei, “Electronic structure and phase stability of MgO, ZnO, CdO, and related ternary alloys”, Phys. Rev. **B77**, 2008, 245209, https://doi.org/10.1103/PhysRevB.77.245209

[16] P. D. C. King, T. D. Veal, A. Schleife, J. Zúñiga-Pérez, B. Martel, P. H. Jefferson, F. Fuchs, V. Muñoz-Sanjosé, F. Bechstedt, and C. F. McConville, “Valence-band electronic structure of CdO, ZnO, and MgO from x-ray photoemission spectroscopy and quasi-particle-corrected density-functional theory calculations”, Phys. Rev., **B79**, 2009, 205205, https://doi.org/10.1103/PhysRevB.79.205205

Chapter 5

Effects of Al doping on the structural, electrical, and optical properties of RS-ZnCdO thin films grown by molecular beam epitaxy

5.1 Introduction

In the previous **Chapter 4**, ZnCdO thin films have grown on MgO [1] substrates by molecular beam epitaxy (MBE). Because the band gap of RS- ZnCdO increases with decreasing Cd content *x* in the alloy, it is important to grow RS-ZnCdO with lower Cd content *x*. Growth on MgO substrates [1] was studied under the assumption that the compositional region would expand by using the RS-MgO structure although the phase stability was not significantly affected by the substrate. However, it was found that single-crystal RS-ZnCdO thin films could be grown on MgO despite the 11.6% lattice mismatch between RS-MgO and RS-CdO, which decreased with decreased Cd content [1]. And an optical band gap of 3.08 eV was obtained in RS-ZnCdO with Cd content x=0.59 on MgO.

Although this optical band gap has been the highest reported value for undoped RS-ZnCdO, it was still lower than those of other TCOs. Because further decreases in Cd content (x<0.59) make it difficult to maintain the RS structure and prevent a transition to the WZ phase, the optical band gap can be increased via a Burstein-Moss shift by increasing in the electron concentration with extrinsic doping. Al has been a widely used donor dopant in ZnO [2], but little has been reported on Al-doping effects in RS-ZnCdO. In this **Chapter 5**, the electrical and optical effects of Al

doping that expands the optical band gap in RS-ZnCdO thin films grown on MgO (100) substrates by increasing the carrier concentration are reported.

5.2 Experimental methods

Al-doped ZnCdO thin films were grown on MgO (100) substrates by a MBE system equipped with a radio-frequency radical cell. The substrates were ultrasonically cleaned in an organic solvent prior to film growth. The background pressure in the growth chamber was less than 6×10^{-8} Pa, and Cd (6N), Zn (7N), and Al (6N) source materials were used. Oxygen radicals were supplied constantly via the radio-frequency cell operating at 300 W and a 0.3-sccm oxygen flow rate. The substrate temperature was maintained at 250 °C during growth, which was previously determined to be optimum for ZnCdO films [1,3].

Firstly, the Al cell temperature was varied over the range 775–950 °C, and the Cd flux ratio (f_{Cd}=[Cd flux]/([Cd flux]+[Zn flux])) was kept constant at 0.96, where single-crystal undoped RS-$Zn_{1-x}Cd_xO$ thin films with x~0.88 were obtained previously [1]. The effects of Al doping for different Cd content by varying the Cd flux ratio over the range 0–1 at a fixed Al cell temperature of 825 °C are investigated.

During MBE growth, the surface crystallinity was monitored with reflection high-energy electron diffraction. The ZnCdO film thickness was measured with a surface step-profiler at a resolution of 0.1 nm. The Cd content x and Al content [=Al/(Zn+Cd+Al)] were determined with energy-dispersive X-ray spectroscopy. The film crystal structures were analyzed with θ–2θ X-ray diffraction (XRD) using a 1.5418-Å Cu Kα source. A double-beam spectrophotometer was used

for reflectance and transmittance measurements over the wavelength range of 200–2000 nm. In the transmittance measurements, a bare MgO substrate was placed in the reference path. The absorption coefficient (α) was obtained via the Beer-Lambert law using the measured reflectance, transmittance, and film thickness. The optical band-gap energies were determined using a previously reported method [4,5]. Electrical properties were characterized with Hall-effect measurements using the Van der Pauw configuration with In ohmic contacts at room temperature.

5.3. Results and discussion

5.3.1 Al-cell-temperature dependence of the crystallinity, Al concentration, and electrical and optical properties in RS-ZnCdO thin films

Figure 5.1(a) plots the Cd and Al contents in Al-doped ZnCdO thin films grown at different Al cell temperatures (T_{Al}). The Cd content in undoped ZnCdO thin films is also shown for comparison. Because the Cd content was very sensitive to slight changes in the Cd flux ratio during growth [1], the Cd content in the Al-doped ZnCdO films was different for samples with x ranging over 0.78– 0.88 for $T_{Al} \leq 900$ °C. The Al content increased monotonically with T_{Al} and was 13% at T_{Al}=900 °C. For $T_{Al} \geq 920$ °C, there was a rapid increase in Al content and a decrease in Cd content.

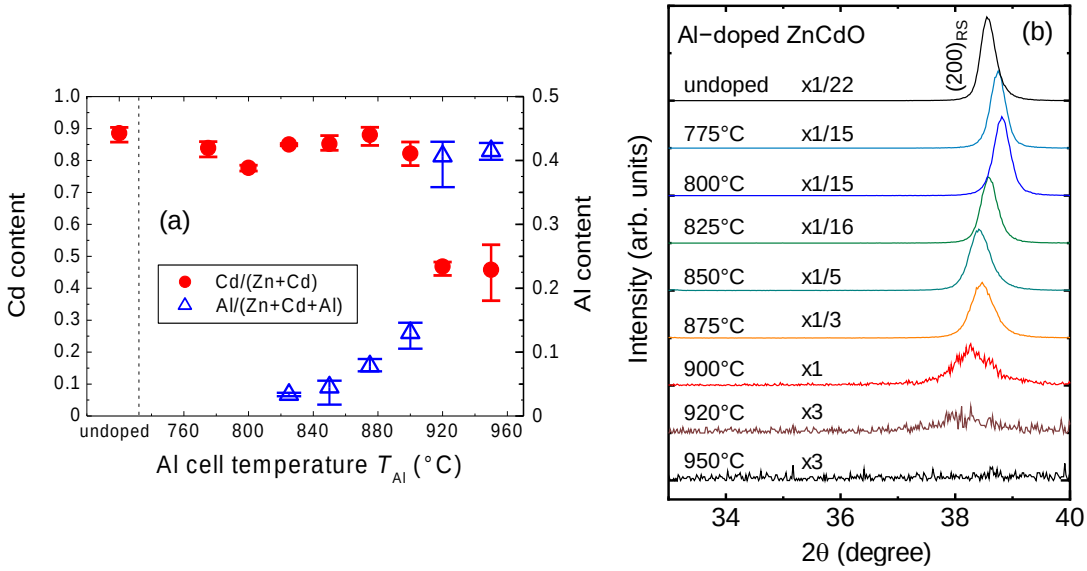

Figure 5.1 (a) Cd and Al contents determined by energy-dispersive X-ray spectroscopy. (b) X-ray diffraction patterns of undoped and Al-doped ZnCdO thin films grown at different Al cell temperatures (T_{Al}).

Figure 5.1(b) shows XRD patterns of undoped and Al-doped ZnCdO thin films. A strong diffraction peak from the RS-ZnCdO (200) plane was observed in undoped ZnCdO. The peak intensity was strong up to T_{Al} =825 °C, and then weakened at T_{Al} ≥850 °C. The peak broadened as T_{Al} increased to 875 °C with the film crystallinity deterioration, and then very weak and broad peak

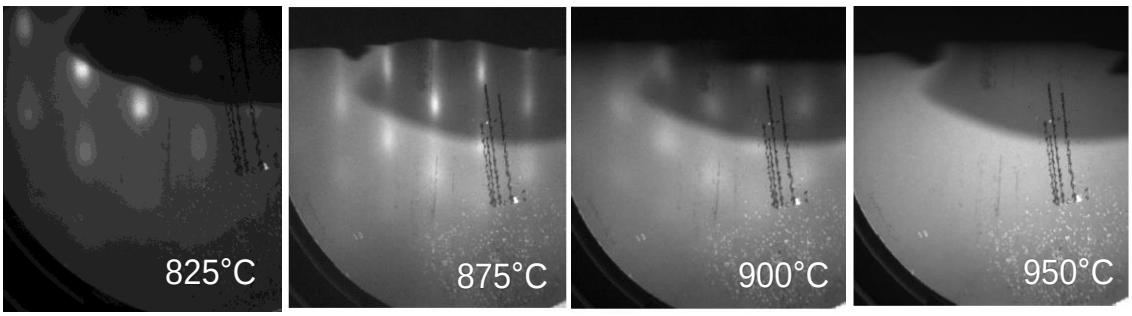

Figure 5.2 Reflection high-energy electron diffraction patterns for Al-ZnCdO thin films grown with various Al cell temperatures

was observed at T_{Al}=900°C. Eventually, the film became amorphous at T_{Al}≥920 °C, with no observable diffraction peak, because of excess Al incorporation. Al-related alloys might be formed at such a high T_{Al}.

Reflection high-energy electron diffraction patterns for Al-doped ZnCdO thin films are shown in Fig. 5.2. A spot pattern was observed for T_{Al} ≤875 °C, indicating epitaxial growth. At T_{Al} =900 °C, the pattern became halo-like with very weak spots, indicating reduced crystallinity. Films grown at T_{Al} =950 °C exhibited a halo pattern corresponding to amorphous structures. These results were thus consistent with the XRD analyses, and the upper limit of T_{Al} for single-crystal Al-doped RS-ZnCdO growth on MgO was 875°C, which corresponded to 7.8% Al content.

Figure 5.3 shows the variation in the electron concentration n and mobility μ in undoped and Al-doped ZnCdO thin films grown at different T_{Al}. The undoped ZnCdO had n~5.0×10^{20}cm^{-3}. For

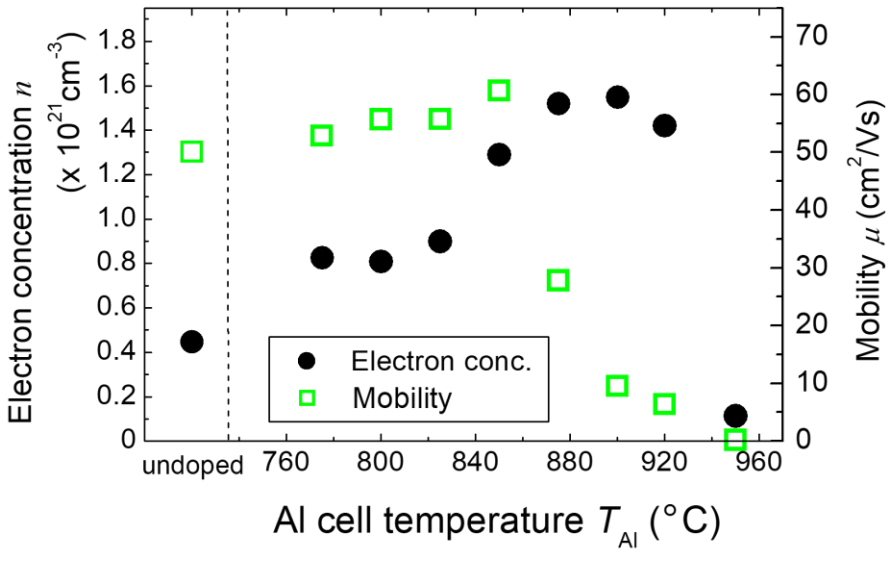

Figure 5.3 Electron concentrations and mobilities of undoped and Al-doped ZnCdO thin films vs. Al cell temperatures.

the Al-doped films, n increased with increasing T_{Al} and was n~1.5×10^{21} cm^{-3} at T_{Al} =875 °C, with 7.8% Al content. For films grown with T_{Al} in the range 825–875 °C, the activation efficiency (ratio of n and Al concentrations) decreased from 73% to 50%. This may be attributed to the energetically favorable formation of native acceptor defects as the Fermi level moved higher up at higher n. The mobilities of all the films grown at T_{Al} ≤850 °C were in the range of 50–60 cm^2/Vs, but decreased abruptly with further increases in T_{Al}. This could be related to compensation by native acceptors and degradation of the crystallinity, as shown in Fig. 5.1(b).

The optical band-gap energies for undoped and Al-doped ZnCdO thin films grown at T_{Al} ≤900 °C are plotted vs. electron concentration in Fig. 5.4. The dependence of the optical band gap energy on electron concentration was calculated by considering FCA effects including the

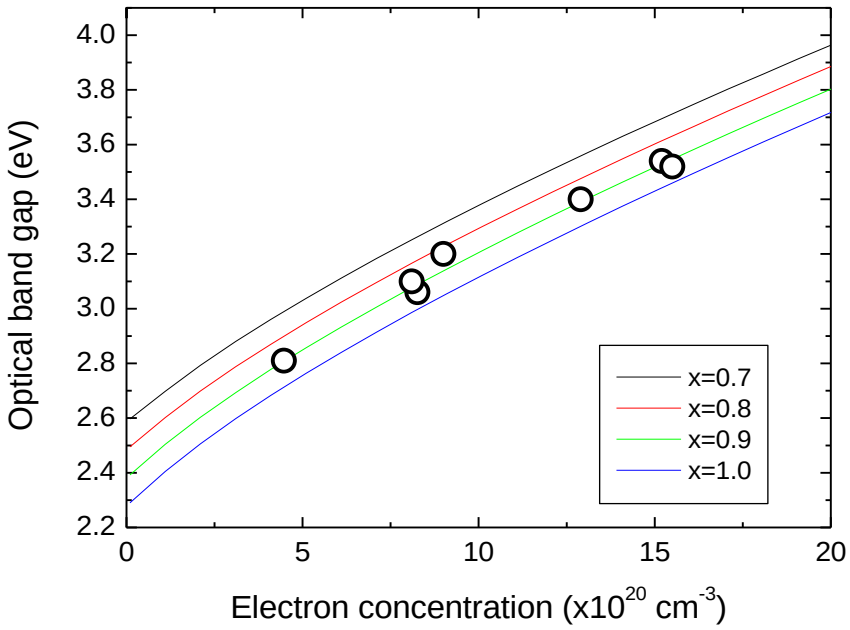

Figure 5.4 Optical band gap energies for undoped and Al-doped ZnCdO thin films grown at T_{Al} ≤900 °C vs. electron concentration. Solid lines are calculated optical band gaps by considering free-carrier absorption including Burstein-Moss shifts and band renormalization.

Burstein-Moss shift and band renormalization, as reported previously [6,7], and are plotted as solid lines for RS-ZnCdO for x=0.7–1.0 in Fig. 5.4. The experimental optical band gap energies were in good agreement with the calculations.

5.3.2 Effects of Al doping on the electrical and optical properties in ZnCdO thin films having various Cd content

To avoid possible deterioration of crystallinity induced by high Al concentrations, we used a moderate T_{Al} =825 °C (Al content of 3.4%) for various Cd contents. The film thicknesses on the MgO (100) substrates were 60±3 nm for all Cd content x. Figure 5.5 (a,b) shows scanning electron microscopy surface images of an Al-doped ZnCdO thin film for Cd content x= 0.61 at 2000× and 8000× magnifications, respectively. The small particle on the surface was In attached during ohmic contact deposition. The thin-film surface was very smooth and clean, indicating no morphological defects.

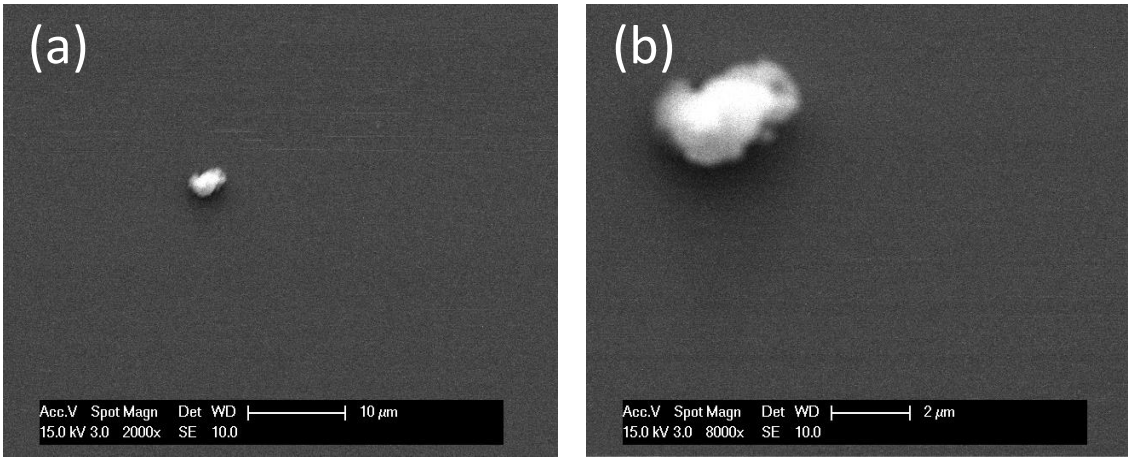

Figure 5.5 Scanning electron microscope images at magnification of (a) 2000× and (b) 8000× times of Al-doped ZnCdO thin film at Cd content x=0.61. A particle of In was attached during ohmic contact deposition.

To investigate the effect of Al doping on the ZnCdO phase stability, XRD analyses were performed, as shown in Fig. 5.6. At x=0, the XRD peak was observed at 2θ=34.4°, which corresponded to diffraction from the (0002) plane of WZ-ZnO. The peak shifted continuously to 33.6° with increasing Cd content up to x=0.54, indicating an increased lattice constant for WZ-ZnCdO because of Zn replacement by the larger Cd.

The WZ (0002) diffraction peak broadened and weakened with further increases in Cd content, and an additional peak appeared at 38.4° that corresponded to (200) diffraction from RS-ZnCdO. Hence, the $0.56 \leq x \leq 0.63$ composition window was a mixed-phase region of WZ- and RS-ZnCdO grains. Similar changes in the diffraction peaks were observed for undoped ZnCdO thin films on MgO (100) substrates [1], but with mixed phases observed at a slightly lower Cd content

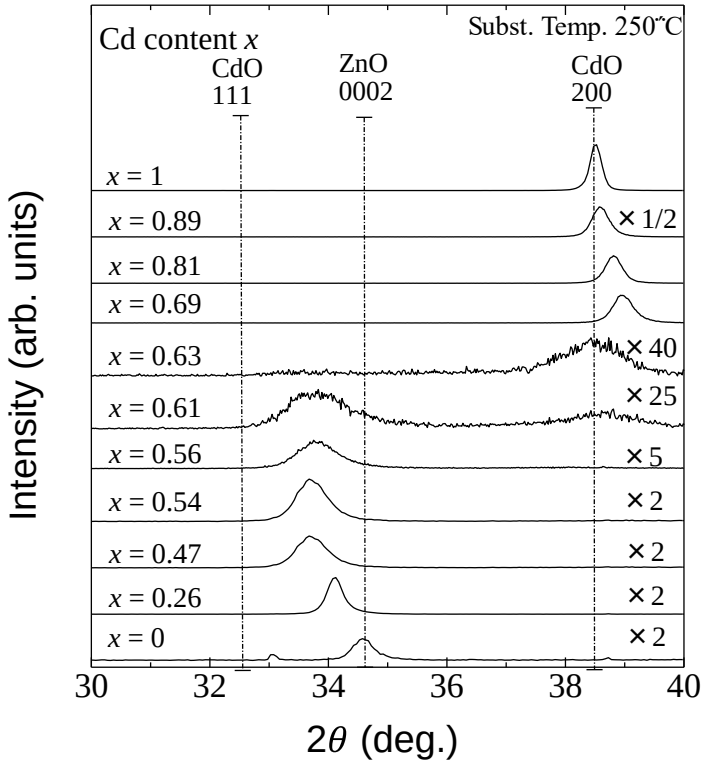

Figure 5.6 X-ray diffraction patterns for Al-doped ZnCdO films with various Cd content.

(0.51≤x≤0.59). Hence, Al doping extended the WZ phase to a slightly richer Cd content. The reason was not clear, but one possibility was that Al doping reduced stress from the incorporated Cd atoms, thus extending the WZ phase. Theoretical calculation such as first-principles density-functional-theory calculations [6] may be required to confirm this.

When x decreased from 1 to 0.69, the RS-ZnCdO (200) diffraction peak angle 2θ shifted from 38.4° to 38.9°, which was consistent with the substitution of smaller Zn atoms in Cd sites forming RS-ZnCdO random alloys. Except for the slight difference in the mixed-phase region, the overall Al-doped ZnCdO composition-dependence of the XRD patterns was similar to previous results for undoped ZnCdO on MgO (100) substrates [1]. Figure 5.7 plots the resistivities ρ (a), electron concentrations n (b), and mobilities μ (c) of Al-doped ZnCdO thin films on MgO (100) as a function of Cd content x. The electrical properties for undoped ZnCdO thin films on MgO (100) are also plotted for comparison. All films, undoped or Al-doped, exhibited n-type conductivity throughout the entire composition range. In the WZ phase region (x<0.56), the resistivity was greatly reduced by Al doping. In particular, at x=0 (ZnO), the resistivity decreased by more than four orders of magnitude after Al doping, and reaches 2.6×10^{-1} Ω-cm because of the

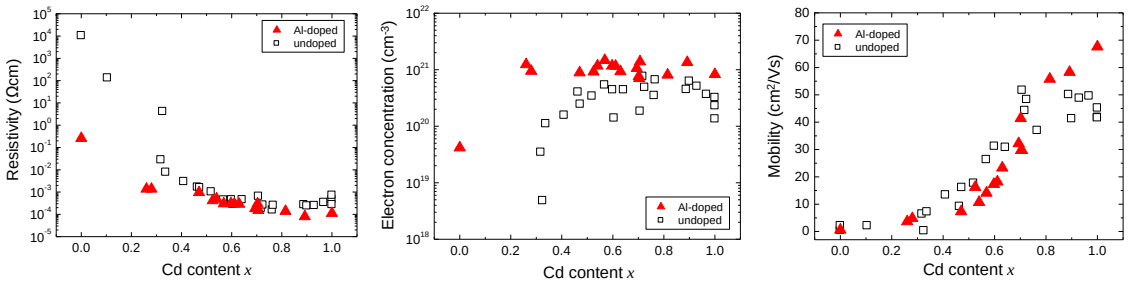

Figure 5.7. (a) Resistivity (b) carrier concentration (c) mobility of Al-doped ZnCdO thin films on MgO (100) vs. Cd content x. Values for undoped ZnCdO thin films are plotted for comparison.

substantial increase in n from 3×10^{14} cm^{-3} to 4×10^{19} cm^{-3}, as shown in Fig. 5.7(b), while the mobility remained essentially constant with Al doping (μ <10 cm^2/V-s). With increasing Cd content to x>0.27, n of the alloy films exceeded 10^{21} cm^{-3} and the resistivity decreased to $<10^{-3}$ Ω-cm. Overall, for the WZ alloys, μ<20 cm^2/Vs.

In the RS phase region (x>0.63), Al-doped RS-ZnCdO films exhibited a low ρ of $(1–2)\times10^{-4}$ Ω-cm, which was lower than that for undoped films. This was attributed to the higher electron concentration of 10^{21} cm^{-3} from Al doping. In addition, the mobility of the Al-doped films was higher, especially for alloys with x>0.8 (≳60 cm^2/V-s).

Transmittance spectra for Al-doped WZ-ZnCdO (x=0.47), mixed-phase ZnCdO (x=0.6), and RS-ZnCdO (x=0.7) are plotted in Fig. 5.8. The RS-ZnCdO (x~0.7) thin film had a transmittance >85% in the visible region (470–700 nm) and >90% in the IR (700–2000 nm). WZ-ZnCdO (x~0.47) and mixed-phase ZnCdO (x~0.6) exhibited slightly lower transmittances over the

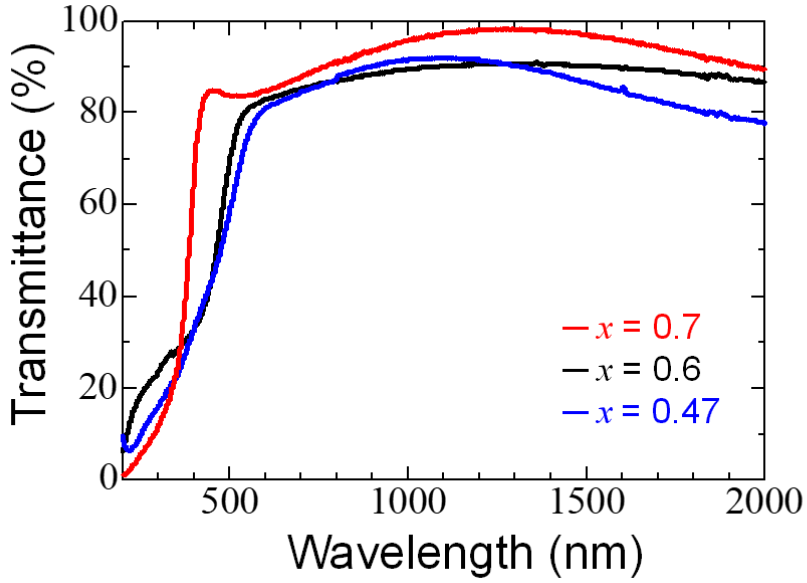

Figure 5.8. Transmittance of Al-doped ZnCdO thin films for x=0.7, 0.6, and 0.47.

entire spectral range. Furthermore, the RS alloy film exhibited a decrease in transmittance at 400 nm, while that for the WZ and mixed-phase alloys decreased at 500 nm. This indicated that the optical absorption edge for RS-ZnCdO was much larger than that for WZ-ZnCdO.

Figure 5.9 shows optical and intrinsic band-gap energies for Al-doped ZnCdO films as a function of Cd content. The intrinsic band-gap energies were obtained by subtracting the high-energy shift from free-carrier effects from the optical band gap energies, as reported previously [6,7]. In Fig. 5.9, the optical band gap energy decreased from 3.43 eV to 2.46 eV in the WZ region with increasing Cd content x from 0 to 0.54, and then increased in the mixed-phase region for $0.56 \leq x < 0.63$. With further increases in Cd content, the gap decreased again from 3.45 eV to 2.8 eV in the RS region. The intrinsic band gap energy of ZnCdO depended on both Cd content and crystal structure [1,3]. For both the WZ and RS phases, the band gap decreased with increasing Cd content, while there was a steep increase of ~1 eV at the WZ-to-RS phase transition. The larger

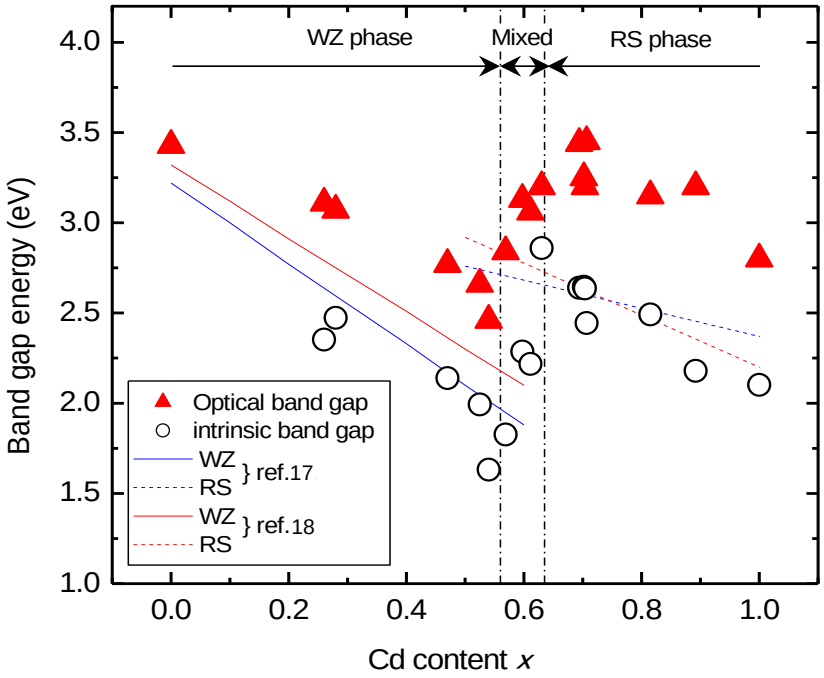

Figure 5.9. Optical and intrinsic band-gap energies of Al-doped ZnCdO thin films with various Cd contents.

RS-ZnCdO band gap was attributed to the weakened *p-d* repulsion between metal d and O *2p* states, because of the forbidden symmetry in RS-ZnCdO [8,9,10,11]. The observed band gap change for ZnCdO was similar to that in previous studies of undoped ZnCdO on sapphire [3] and MgO (100) substrates [1]. However, the optical band-gap energy of RS-ZnCdO was larger than that of undoped samples because of the high electron concentration. In particular, at $x \approx 0.7$, RS-ZnCdO alloy films had an optical band gap energy of 3.45 eV, with a very low resistivity of 1×10^{-4} Ω-cm, and a wide transmission window of up to 2000 nm.

Low-resistivity and good-transmissivity single-crystal RS-ZnCdO films on MgO (100) could be applicable to high-efficiency multi-junction solar cells that often use cubic-crystal GaAs (100) or Ge (100) substrates. Ashrafi et al. reported single-crystal growth of CdO layers on GaAs (100) [12]. Similar epitaxial growth of RS-ZnCdO is expected on GaAs (100). Hence, Al doping in RS-ZnCdO films could be effective TCOs for devices utilizing the entire solar spectrum.

5.4. Conclusions

Effects of Al doping on the structural, electrical, and optical properties of RS-ZnCdO thin films on MgO substrates were investigated. The highest T_{Al} at which single-crystal growth of Al-doped RS-ZnCdO with $x \approx 0.83$ is possible was determined to be 875 °C, which corresponded to an Al-doping concentration of ~7.8%. The electron concentration increased with Al doping at increased T_{Al}, and was $n \sim 1.5\times10^{21}$ cm^{-3} at T_{Al} = 875 °C. The corresponding optical band gap energy increased because of free-carrier effects including Burstein-Moss-shift and band-renormalization. Furthermore, Al was an efficient donor dopant in both RS-ZnCdO and WZ-ZnCdO thin films.

Electron concentrations $>10^{21}$ cm^{-3} were obtained with Al doping for alloys incorporating Cd content *x* ranging from 0.27 to 1.0, regardless of the crystal structure. A large optical band gap energy of 3.45 eV was observed in the RS-ZnCdO thin film having $x \approx 0.7$, with a resistivity of 1×10^{-4} Ω-cm, and a wide transmission window of up to 2000 nm. Thus, the film was an applicable transparent conductor for full solar spectrum solar cells.

Reference

[1] H. C. Jang, , K. Saito, Q. Guo, K. M. Yu, W. Walukiewicz, T. Tanaka, "Structural, optical, and electrical properties of WZ- and RS-ZnCdO thin films on MgO (100) substrate by molecular beam epitaxy", J. Alloys and compounds, **867**, 2021, 159033, https://doi.org/10.1016/j.jallcom.2021.159033

[2] C. G. Granqvist, "Transparent conductors as solar energy materials: A panoramic review", Sol. Energy Mater. Sol. Cells, **91**, 2007, 1529–1598, https://doi.org/10.1016/j.solmat.2007.04.031

[3] H. C. Jang, K. Saito, Q. Guo, K. M. Yu, W. Walukiewicz, T. Tanaka, "Realization of rocksalt $Zn_{1-x}Cd_xO$ thin films with optical band gap above 3.0 eV by molecular beam epitaxy", CrystEngComm. **22**, 2020, 2781, https://doi.org/10.1039/C9CE02018G

[4] A. Dolgonos, T. O. Mason, K. R. Poeppelmeier, "Direct optical band gap measurement in polycrystalline semiconductors : A Critical Look at the Tauc Method", J. Solid State Chemistry, **240**, 2016, 43. https://doi.org/10.1016/j.jssc.2016.05.010

[5] C. Y. Ho, C. P. Liu, Y. C. Chen, Z. Q. Huang, F. C. Chuang, and K. M. Yu, "Effects of oxygen stoichiometry on the phase stability of sputter deposited $Cd_xZn_{1-x}O$ alloys", Phys. Rev. Materials, **3**, 2019, 074605, https://doi.org/10.1103/PhysRevMaterials.3.074605

[6] K. M. Yu, M. A. Mayer. D. T. Speaks, H. He, R. Zhao, L. Hsu, S. S. Mao, E. E. Haller, W. Walukiewicz, "Ideal transparent conductors for full spectrum photovoltaics", J. Appl. Phys., **111**, 2012, 123505, https://doi.org/10.1063/1.4729563

[7] D. M. Detert, K. B. Tom, C. Battaglia, J. D. Denlinger, S. H. N. Lim, A. Javey, A. Anders, O. D. Dubon, K. M. Yu, W. Walukiewicz, "Crystal structure and properties of $Cd_xZn_{1-x}O$ alloys across the full composition range", Appl. Phys. Lett. **102**, 2013, 232103. https://doi.org/10.1063/1.4809950

[8] A. Schleife, F. Fuchs, J. Furthmüller, F. Bechstedt, "First-principles study of ground- and excited-state properties of MgO, ZnO, and CdO polymorphs", Phys. Rev., **B73**, 2006, 245212, https://doi.org/10.1103/PhysRevB.73.245212

[9] S.H. Wei, A. Zunge, "Role of metal d states in II–VI semiconductors", Phys. Rev., **B37**, 1988, 8958–8981, https://doi.org/10.1103/PhysRevB.37.8958

[10] Y.Z. Zhu, G.D. Chen, H.G. Ye, A. Walsh, C.Y. Moon, S.H. Wei, "Electronic structure and phase stability of MgO, ZnO, CdO, and related ternary alloys", Phys. Rev., **B77**, 2008, 245209, https://doi.org/10.1103/PhysRevB.77.245209

[11] P.D.C. King, T.D. Veal, A. Schleife, J. Zúñiga-Pérez, B. Martel, P.H. Jefferson, F. Fuchs, V. Muñoz-Sanjosé, F. Bechstedt, C.F. McConville, "Valence-band electronic structure of CdO, ZnO, and MgO from x-ray photoemission spectroscopy and quasi-particle-corrected density-functional theory calculations", Phys. Rev., **B79**, 2009, 205205, https://doi.org/10.1103/PhysRevB.79.205205.

[12] A. B. M. A. Ashrafi, H. Kumano, and I. Suemune, "Single-crystalline rocksalt CdO layers grown on GaAs (001) substrates by metalorganic molecular-beam epitaxy", Appl. Phys. Lett., **79**, 470, 2001, https://doi.org/10.1063/1.1387258.

Chapter 6

Summary

ZnCdO thin films have attracted as considerable materials for gas sensors, photocatalysts, and TCOs. Significantly, the brilliant optical and electrical properties of ZnCdO make it as a considerable TCO candidate for full spectrum solar cells or MJSCs. The transparent window width (420~2000 nm) and high transmittance (≥ 80%) of ZnCdO thin films enables the solar cell to absorb much more sun spectrum, archiving higher conversion efficiency. The excellent electrical properties of low resistivity ($\leq 1 \times 10^{-4}$ Ωcm) and high mobility (≥ 60 cm^2/Vs) of ZnCdO thin films lead this material not only for TCO application but also for other optoelectronic devices.

The purpose of this study is to investigate the growth mechanism and characterization of the ZnCdO thin films on sapphire and MgO substrate by MBE. Also, the way to expand the band gap energy of ZnCdO thin films are investigated by Al doping. The results obtained in this study are summarized as follows.

In **Chapter 3**, ZnCdO thin films were grown on α-Al_2O_3 (0001) substrate by MBE with various Cd content. The phase transition from wurtzite to rocksalt is found to take a place at the Cd content x ~ 0.5 to 0.6. Within the composition region of x ~ 0.5 to 0.6, both RS and WZ crystals co-exist. Transmittance above 80 ~ 95 % in the visible range is observed for both the WZ and RS alloys. Optical gap of the WZ alloys decreases from 3.27 eV for ZnO to ~ 2.35 eV (x ~ 0.44). At the phase transition to RS at x ~ 0.55, the optical gap increases drastically to > 3.0 eV RS-alloys with a large optical gap of 3.0 eV (an intrinsic gap of ~ 2.7 eV) is achieved for x ~ 0.6. RS-ZnCdO

thin films exhibit a low resistivity of 5×10^{-4} Ωcm with maximum mobility of ~ 90 cm^2/Vs and a high carrier concentration 4×10^{20} cm^{-3}.

In **Chapter 4**, ZnCdO thin films with various Cd compositions were grown on MgO (100) substrates by MBE. It was found that the phase transition from WZ to RS occurs at the Cd composition x between 0.51 and 0.59. In the visible range, high transmittance above 85% was observed for RS-ZnCdO films ($0.59 \leq x \leq 1.0$). In the WZ-phase region, the optical band gap energy decreased from 3.25 eV for ZnO to ~ 2.16 eV for WZ-ZnCdO with x ~ 0.51. After the partial phase transition from WZ to RS at $x > 0.51$, the optical band gap energy increased intensely and the largest optical band gap energy of 3.08 eV was obtained for x =0.59 with an intrinsic band gap energy of 2.72 eV. RS-ZnCdO films showed a low resistivity around 2.5×10^{-4} Ωcm with a maximum mobility of ~ 51.7 cm^2/Vs and a high carrier concentration around 5×10^{20} cm^{-3}. These characteristics of RS-ZnCdO are attractive as TCO materials in future full spectrum solar cells.

In **Chapter 5**, effects of Al doping on the structural, electrical, and optical properties of RS-ZnCdO thin films on MgO substrates were investigated. The highest T_{Al} at which single-crystal growth of Al-doped RS-ZnCdO with $x \approx 0.83$ is possible was determined to be 875 °C, which corresponded to an Al-doping concentration of ~7.8%. The electron concentration increased with Al doping at increased T_{Al}, and was $n \sim 1.5 \times 10^{21}$ cm^{-3} at T_{Al} = 875 °C. The corresponding optical band gap energy increased because of free-carrier effects including Burstein-Moss-shift and band-renormalization. Furthermore, Al was an efficient donor dopant in both RS-ZnCdO and WZ-ZnCdO thin films. Electron concentrations $>10^{21}$ cm^{-3} were obtained with Al doping for alloys incorporating Cd content x ranging from 0.27 to 1.0, regardless of the crystal structure. A large optical band gap energy of 3.45 eV was observed in the RS-ZnCdO thin film having $x \approx 0.7$, with a

resistivity of 1×10^{-4} Ω-cm, and a wide transmission window of up to 2000 nm. Thus, the film was an applicable transparent conductor for full solar spectrum solar cells.

Table 6.1 show the summary of Chapter 3,4 and 5. The results obtained in this study demonstrate that low-resistivity and good-transmissivity single-crystal RS-ZnCdO films on MgO (100) could be applicable to high-efficiency multi-junction solar cells that often use cubic-crystal GaAs (100) or Ge (100) substrates.

Table 6.1 Summary of **Chapter 3, 4** and **5**.

	Phase	High transmittance (over 80%)	Highest optical band gap	Resistivity	Mobility	Carrier concentration
Chapter 3 : undoped ZnCdO on sapphire substrate	WZ : $x > 0.5$ RS : $x < 0.6$	from 500nm	3.0 eV (intrinsic band gap - 2.7 eV)	~ 5×10^{-4} Ωcm	~ 90 cm^2/Vs	~ 4×10^{20} cm^{-3}
Chapter 4 : undoped ZnCdO on MgO substrate	WZ : $x > 0.51$ RS : $x < 0.59$	from 490nm	3.08 eV (intrinsic band gap - 2.72 eV)	~ 2.5×10^{-4} Ωcm	~ 51.7cm^2/Vs	~ 5×10^{20} cm^{-3}
Chapter 5 : Al-doped ZnCdO on MgO substrate	WZ : $x > 0.56$ RS : $x < 0.63$	from 470nm	3.45 eV (intrinsic band gap - 2.8 eV)	~ 10^{-4} Ωcm	~ 60 cm^2/Vs	~ 10^{21} cm^{-3}

Acknowledgements

First of all, I would like to express my sincerest gratitude to my ***Professor Dr. Tooru Tanaka***, Department of Electrical and Electronic Engineering, Saga University for supervising this study and indispensable and expert leadership, valued and constructive suggestions, plentiful support, endless encouragement, metallic supporting during my research work. Without his encouragement and support, I could not complete and present this thesis and study.

I also would like to express my deepest gratitude to ***Professor Qixn Guo***, Synchrotron Light Application Center, Saga University, Japan, for his generous support, suggestions, and encouragements during this research work.

I would like to expand my appreciation to ***Professor Dr. Toshiyuki Oishi***, Department of Electrical and Electronic Engineering, Saga University, and ***Professor Dr. Kazutoshi Takahashi***, Synchrotron Light Application Center, Saga University, Japan, for their generous recommendations and advise on this research work.

Sincere thanks to my respected teacher ***Assistant Professor Dr. Katsuhiko Saito***, Synchrotron Light Application Center, Saga University, Japan, for his suggestions, guidance, and experimental support as well as during various experiments.

I am highly grateful to ***Professor Dr. Kin Man Yu***, Department of Physics and Materials Science, City University of Hong Kong, Kowloon, Hong Kong, for his valuable advice, collaborative support, support for revising papers, and inspiration throughout my research work.

I would like to express my deep sense of gratitude to ***Professor Dr. Wladek Walukiewicz***, Materials Sciences Division, Lawrence Berkeley National Laboratory and Department of Materials Science and Engineering, University of California, USA for his advice, collaborative support, and encouragement.

I would like to express thanks to ***Associate Professor Dr. Md. Abdul Majed Patwary***, Department of Chemistry, Comilla University, Bangladesh for his advice, encouragement, and support.

Lastly, I would like to express my deep appreciation to my family for their encouragement and endless support during my whole study.

List of publications

1. Original Papers Related To This Dissertation

1. HyoChang Jang, Katsuhiko Saito, Qixin Guo, Kin Man Yu, Wladek Walukiewicz, and Tooru Tanaka, Realization of rocksalt $Zn_{1-x}Cd_xO$ thin films with optical band gap above 3.0 eV by molecular beam epitaxy, CrystEngComm., **22**, 2020, 2781-2787.

2. HyoChang Jang, Katsuhiko Saito, Qixin Guo, Kin Man Yu, Wladek Walukiewicz, and Tooru Tanaka, Structural, Optical, and Electrical properties of WZ- and RS-ZnCdO thin films on MgO (100) substrate by molecular beam epitaxy, Journal of Alloys and Compounds, **867**, 2021, 159033(1~6).

3. HyoChang Jang, Katsuhiko Saito, Qixin Guo, Kin Man Yu, and Tooru Tanaka, Effects of Al doping on the structural, electrical, and optical properties of rock-salt ZnCdO thin films grown by molecular beam epitaxy, Journal of Physics and Chemistry of Solids, **163**, 2022, 110571(1~6).

2. Original papers of Other Subjects

1. Kazutoshi Takahashi, Masaki Imamura, Hyochang Jang, Tooru Tanaka, Katsuhiko Saito, Qixin Guo, Kin Man Yu, Wladek Walukiewicz, Three-dimensional band structure and surface electron accumulation of rs-$Cd_xZn_{1-x}O$ studied by angle-resolved photoemission spectroscopy, Sci Rep, **9**, 2019, 8026.

2. M. A. Hossain, S. F. U. Farhad, N. I. Tanvir, J. H. Chang, M. A. Rahman, T. Tanaka, Q. Guo, J. Uddin, M. A. M. Patwary, 2021, Facile synthesis of Cu2O nanorods in the presence of NaCl by SILAR method and its characterizations, Dryad, 2022.

Conference proceedings

1. HyoChang Jang, Katsuhiko Saito, Qixin Guo, and Tooru Tanaka, Growth and characterization of ZnCdO thin films on MgO(100) substrates by MBE, 16th Symposium on Next Generation Solar Power Systems, July 4, 2019

2. HyoChang Jang, Katsuhiko Saito, Qixin Guo, Tooru Tanaka, Kin Man Yu, Wladek Walukiewicz, Growth and characterization of Al-doped rs-ZnCdO thin films on MgO(100) substrates by molecular beam epitaxy, Materials Research Meeting 2019, December 10, 2019.

3. HyoChang Jang, Katsuhiko Saito, Qixin Guo, and Tooru Tanaka, Influence of oxygen flow rate on properties of Al-doped ZnCdO thin films grown by radical-source molecular beam epitaxy, 4th Asian-APC, November 23, 2019.

4. HyoChang Jang, Katsuhiko Saito, Qixin Guo, and Tooru Tanaka, Improved properties of low-resistive Al-doped ZnCdO thin films by MBE, The 67th JSAP spring metting 2020, March 12, 2020.

5. HyoChang Jang, Katsuhiko Saito, Qixin Guo, Tooru Tanaka, Kin Man Yu, Wladek Walukiewicz, Growth of low resistive Al-doped ZnCdO thin films with rocksalt structure for Transparent Conductive Oxide Thin Films, 2020 IEEE 47th PVSC, June 15, 2020.

6. HyoChang Jang, Katsuhiko Saito, Qixin Guo, Kin Man Yu, Wladek Walukiewicz, and Tooru Tanaka, HIGH TRNASMITTANCE TRANSPARENT CONDUCTIVE OXIDES OF ROCKSALT-AL-DOPED ZNCDO FOR FULL SPECTRUM SOLAR CELLS, PVSEC30, November 8, 2020.

7. HyoChang Jang, Katsuhiko Saito, Qixin Guo, and Tooru Tanaka, Influence of oxygen flow rate during the growth of Al-doped ZnCdO thin films by MBE, 68th Spring Academic Lecture of JSAP 2021, March 16, 2021.

8. HyoChang Jang, Katsuhiko Saito, Qixin Guo, and Tooru Tanaka, Growth and characterization of Al-doped and undoped $Zn_{1-x}Cd_xO$ by molecular beam epitaxy under high oxygen flow rate, The 6th Asian Applied Physics Conference (Asian-APC), December 4, 2021.